Determining the stiffness of the equation of state using low T/W dynamical instabilities in differentially rotating stars

Motoyuki Saijo*

Research Institute for Science and Engineering, Waseda University, Shinjuku, Tokyo 169-8555, Japan

(Received 7 May 2018; published 2 July 2018)

We investigate the nature of low T/W dynamical instabilities in various ranges of the stiffness of the equation of state in differentially rotating stars. Here T is the rotational kinetic energy, while W is the gravitational binding energy. We analyze these instabilities in both a linear perturbation analysis and a three-dimensional hydrodynamical simulation. An unstable normal mode of a differentially rotating star is detected by solving an eigenvalue problem along the equatorial plane of the star. The physical mechanism of low T/W dynamical instabilities is also qualitatively confirmed by a scattering of sound waves between corotation and the surface caused by the corotation barrier. Therefore, we can draw a picture of existing pulsation modes unstabilized due to an amplified reflection of sound waves from the corotation barrier. The feature in the eigenfrequency and eigenfunction of the unstable mode in the linear analysis roughly agrees with that in the three-dimensional hydrodynamical simulation in Newtonian gravity. Moreover, the nature of the eigenfunction that oscillates between corotation and the surface for an unstable star requires reinterpretation of pulsation modes in differentially rotating stars. Finally, we propose a manner by which to constrain the stiffness of the equation of state by the direct detection of mode decomposed gravitational waveforms.

DOI: 10.1103/PhysRevD.98.024003

I. INTRODUCTION

Low T/W dynamical instabilities in differentially rotating stars have been found numerically around the 21st century [1–4]. Here T is the rotational kinetic energy, while W is the gravitational binding energy. In contrast to the standard nonaxisymmetric rotational dynamical $m = 2$ bar instability (the threshold is $T/W = 0.2738$ for a uniformly rotating, incompressible star [5–7], toroidal modes $e^{im\varphi}$, where $m = \pm 1, \pm 2, \ldots$, φ is the azimuthal angle), a star becomes dynamically unstable in a significantly low magnitude of rotation when these instabilities set in. A star also becomes dynamically unstable to the $m = 1$ spiral mode [2,4], which has never been found in a rotating stellar configuration. According to plenty of results from numerical simulations, a moderate degree of a differentially rotating configuration of the star is at least required to trigger these instabilities, and the stiffness of the equation of state changes the dominant behavior of these instabilities between spiral and bar [4,8] (except for Ref. [9]).

There are two representative cases of astrophysical applications to low T/W dynamical instabilities. One is the binary neutron star mergers. After the merger, a moderate degree of a differentially rotating configuration can be generated in a dynamical timescale, which may trigger these instabilities. Recent numerical simulations have found a spiral type of configuration after the merger (see, e.g., [10–13]), and found the angle direction changes in a constant phase curve [10,11], which may be essentially the same as that in $m = 1$ low T/W dynamical instabilities [8]. The other is the collapse driven supernovae. After the core bounce, a proto-neutron star with a high degree of differential rotation (see, e.g., [14,15]) can be generated in a dynamical timescale. In such a case, requirements for triggering these instabilities are naturally satisfied. In fact, the $m = 1$ instabilities of gravitational waveforms in collapse driven supernovae have been demonstrated (see, e.g., [16]).

In contrast to a clear existence of low T/W dynamical instabilities, a physical mechanism to trigger them is still a mystery. The main issue comes from the fact that there is no complete successful multidimensional linear perturbation analysis in differentially rotating stars. At present, there are two representative discussions about the necessary conditions to trigger these instabilities and their demonstrations, mainly based on a self-gravitating disk system. One is the corotation resonance, which originally comes from the density wave theory that a self-gravitating disk becomes unstable due to the absorption of angular momentum at corotation (see, e.g., [17]). Since corotation plays an essential role in a disk system, a characteristic feature of corotation to these instabilities in basic equations has been argued [18]. Comparison between low T/W dynamical instabilities and standard $m = 2$ ones based on a canonical

*saijo@aoni.waseda.jp

angular momentum distribution has been discussed [8]. The other is nonaxisymmetric Rossby wave instabilities, which have been investigated for finding a necessary condition where a potential vorticity takes an extreme [19]. The necessary conditions acquired in a disk system have been applied to low T/W dynamical instabilities [9,20]. However, no multidimensional linear perturbation analysis has been done so far in a rotating stellar configuration. Such an analysis is necessary since both a rotating stellar configuration and a self-gravitating effect may take place (but see Refs. [3,21,22] for a specific fundamental mode of pulsating stars). Without the analysis mentioned above, it would not be possible to completely understand the physical mechanism of low T/W dynamical instabilities.

The purpose of this paper is threefold. First, we want to understand physical features of low T/W dynamical instabilities by both linear analyses and numerical simulations. Although plenty of numerical simulations have confirmed the existence of their instabilities, understanding their features, such as extracting functional dependence of characteristic frequencies and timescales, is extremely expensive solely by numerical simulations. At least, large parameter sets of computations are required. On the other hand, a full set of linear perturbation analysis in differentially rotating stars requires two spatial dimensional analyses even when we adopt harmonic expansion for time and azimuthal angle. It is still in progress in a general manner even in Newtonian gravity (see, e.g., [21,23]). But instead of exploring these instabilities in a two-dimensional linear perturbation analysis, we restrict our analysis to the equatorial motion of a perturbed fluid, taking a self-gravitating effect into account. Although this is a crude assumption we impose in our study [24,25], it would still be useful for finding some physical aspects of these instabilities by combining two complementary approaches. This part is an extension work of Ref. [24] for a wide set of parameters, each of which varies the stiffness of the equation of state.

Second, we want to understand the physical mechanism of low T/W dynamical instabilities. Computational results from three-dimensional hydrodynamical simulations are sufficiently attractive to understand the dynamical features of their instabilities, but without sophisticated diagnostic quantities and plenty of parameter searches, it is extremely difficult to confirm the physical mechanisms by themselves. Although a linear analysis can only apply to the linear stage of the instability growth, it is quite powerful to identify the specific features of these instabilities. Our idea is to investigate the linear analysis in these systems and acquire a picture for generating these instabilities. Such a picture could be useful for a deeper understanding of these instabilities by three-dimensional numerical simulations. Although the idea of a scattering problem by the corotation barrier has been introduced in Ref. [25], we have improved and adjusted the analysis by comparing the results of linear analyses with those of three-dimensional numerical simulations.

Finally, we focus on gravitational waves generated from these instabilities. Nonaxisymmetric instabilities are subject to quasiperiodic gravitational waves in general. In principle, these gravitational waves can be detected in ongoing ground-based detectors such as advanced LIGO, advanced VIRGO, KAGRA, and future projects such as Einstein Telescope [26]. All detectors have good sensitivity around kilohertz frequencies, preparing for exploring the dynamics of neutron stars. In fact, recent detection of the merger of binary neutron stars has opened a new era for exploring neutron stars by gravitational waves [27]. Detailed analysis of gravitational waveforms may tell us a variety of interior features of neutron stars, and it would be worth investigating gravitational waveforms and their spectra of these instabilities from a theoretical viewpoint. Moreover, we propose a method to constrain the stiffness of the equation of state from the direct observation of gravitational waves, which would potentially become a guideline for future realistic astrophysical simulations, direct observations, and data analyses for extracting physics.

The content of this paper is as follows. In Sec. II, we briefly explain the basic hydrodynamic equations in Newtonian gravity equipping shock capturing schemes in our code with a code test. In Sec. III, we introduce our basic equations of perturbative approaches and our formulation of a normal mode analysis and a scattering problem rising from the corotation barrier, as well as their results. In Sec. IV, we show our results of three-dimensional numerical simulations and compare them with those of perturbative approaches and gravitational waves from low T/W dynamical instabilities. Section V is devoted to the summary of this paper. Throughout this paper, we use the geometrized units with $G = c = 1$ [28].

II. HYDRODYNAMICS

A. Basic equations

We summarize here the basic equations for perfect fluids of hydrodynamics in Newtonian gravity. We assume an adiabatic Γ-law equation of state

$$p = (\Gamma - 1)\rho\varepsilon, \tag{2.1}$$

where p is the pressure, Γ the adiabatic index, ρ the rest mass density, and ε the specific internal energy density. For perfect fluids, Newtonian equations of hydrodynamics consist of the continuity equation

$$\frac{\partial \rho}{\partial t} + \frac{\partial(\rho v^j)}{\partial x^j} = 0, \tag{2.2}$$

where v^i is the velocity, the energy equation

$$\frac{\partial e}{\partial t}+\frac{\partial[(e+p)v^j]}{\partial x^j}=-\rho v^j\frac{\partial\Phi}{\partial x^j}, \tag{2.3}$$

where $e=\rho(\varepsilon+v_jv^j/2)$ is the total energy, and the Euler equations

$$\frac{\partial(\rho v^i)}{\partial t}+\frac{\partial(\rho v^iv^j+p\delta^{ij})}{\partial x^j}=-\rho\frac{\partial\Phi}{\partial x^i}, \tag{2.4}$$

where Φ is the gravitational potential, which satisfies

$$\triangle\Phi=4\pi\rho. \tag{2.5}$$

Constructing the equilibrium configuration of a differentially rotating star assuming a polytropic equation of state $p=\kappa_s\rho^\Gamma$ with κ_s being constant, first we have to solve the Euler equations. In the axisymmetric configuration, the equation can be described in the cylindrical coordinates as

$$\frac{1}{\rho}\nabla_\varpi p+\nabla_\varpi\Phi-\varpi\Omega^2=0, \tag{2.6}$$

where ϖ is the cylindrical radius and Ω the angular velocity. Here we adopt j-constant rotation law for the angular velocity distribution of the star as

$$\Omega=\frac{j_0}{d^2+\varpi^2},$$

where j_0 is the constant and d the degree of differential rotation. With this rotation law, we can integrate Eq. (2.6) as

$$H+\Phi+\Phi_c=C, \tag{2.7}$$

where the enthalpy H and the rotational potential Φ_c are

$$H=\varepsilon+\frac{p}{\rho}, \tag{2.8}$$

$$\Phi_c=-\int^\varpi\varpi\Omega^2d\varpi=\frac{1}{2}\frac{j_0^2}{d^2+\varpi^2}, \tag{2.9}$$

n is the polytropic index with a relation $\Gamma=1+1/n$, and C is the constant. We summarize our configuration of differentially rotating stars in Table I.

TABLE I. Equilibrium configuration of differentially rotating stars.

Model	n	Ω_c/Ω_e[a]	T/W
I(a)	1	26.0	6.09×10^{-2}
I(b)	1	12.1	8.00×10^{-2}
I(c)	1	5.0	1.00×10^{-1}
I(d)	1	2.0	1.09×10^{-1}
II(a)	1.5	26.0	6.76×10^{-2}
II(b)	1.5	12.1	8.61×10^{-2}
II(c)	1.5	5.0	1.01×10^{-1}
II(d)	1.5	2.0	9.37×10^{-2}
III(a)	2	26.0	7.29×10^{-2}
III(b)	2	12.1	8.89×10^{-2}
III(c)	2	5.0	9.38×10^{-2}
III(d)	2	2.0	6.48×10^{-2}
IV(a)	3	26.0	7.21×10^{-2}
IV(b)	3	12.1	6.89×10^{-2}
IV(c)	3	5.0	4.21×10^{-2}
IV(d)	3	2.0	1.81×10^{-2}

[a]Ω_c: Central angular velocity; Ω_e: Equatorial surface angular velocity.

B. Shock capturing scheme and wall shock tests

Here we review the shock capturing scheme inserted in our Newtonian hydrodynamics code. The flux conservative form of the continuity equation, the Euler equations, and the energy equation can be written as

$$\frac{\partial}{\partial t}\boldsymbol{\mathcal{U}}+\frac{\partial}{\partial x^j}\boldsymbol{\mathcal{F}}^j=\boldsymbol{\mathcal{S}}, \tag{2.10}$$

where the state vector $\boldsymbol{\mathcal{U}}$, the flux vectors $\boldsymbol{\mathcal{F}}^j$, and the source vector $\mathcal{S}$ are

$$\boldsymbol{\mathcal{U}}=\begin{bmatrix}\rho\\ \rho v^i\\ e\end{bmatrix},\qquad \boldsymbol{\mathcal{F}}^j=\begin{bmatrix}\rho v^j\\ \rho v^iv^j+p\delta^{ij}\\ (e+p)v^j\end{bmatrix},$$
$$\boldsymbol{\mathcal{S}}=\begin{bmatrix}0\\ -\rho\frac{\partial\Phi}{\partial x^i}\\ -\rho v^j\frac{\partial\Phi}{\partial x^j}\end{bmatrix}. \tag{2.11}$$

We use a monotonized central-difference (MC) limiter [29] for interpolating the conservative quantities on the grid to the numerical cell boundaries. To respect their thermodynamical properties, we choose ρ, v^i, and ε as primitive quantities. For given primitive variables u_k ($\equiv[\rho_k, v^i_k, \varepsilon_k]$, k: label of grid point), we are able to interpolate the quantities to the left and right intercell boundaries located at $k\pm1/2$. We use the second-order accuracy with monotonic piecewise linear slopes along the coordinate x_k as

$$u^R_{k-1/2}=u_k+\sigma_k(x_{k-1/2}-x_k),$$
$$u^L_{k+1/2}=u_k+\sigma_k(x_{k+1/2}-x_k),$$

where

$$\sigma_k=\mathrm{minmod}\left[2\left(\frac{\Delta u_k}{\Delta x_k}\right),2\left(\frac{\Delta u_{k+1}}{\Delta x_{k+1}}\right)\right], \tag{2.12}$$

$\Delta u_k\equiv u_k-u_{k-1}$, $\Delta x_k\equiv x_k-x_{k-1}$ is the grid separation, and

$$\text{minmod}[a,b] = \begin{cases} 0 & ab \le 0, \\ \text{sgn}(a)\min\left[2|a|, 2|b|, \left(\frac{|a+b|}{2}\right)\right] & \text{otherwise.} \end{cases}$$

Note that the label L and R, respectively, represent the left and right sides of intercell boundaries located at $k \pm 1/2$.

We adopt the approximate Harten-Lax–van Leer (HLL) Riemann solver [30] for constructing a numerical flux

$$F^j_{\rm HLL} = \frac{S^j_R F^j_L - S^j_L F^j_R + S^j_L S^j_R (U^j_R - U^j_L)}{S^j_R - S^j_L}, \tag{2.13}$$

where $F^j_{L,R}$ are the flux vectors at the left and right numerical cells, and $S^j_{L,R}$ are the characteristic speeds at the left and right intercell boundaries determined as

$$S^j_L = \max(0, \lambda^{j+}_L, \lambda^{j+}_R, v^j_L, v^j_R), \tag{2.14}$$

$$S^j_R = \min(0, \lambda^{j-}_L, \lambda^{j-}_R, v^j_L, v^j_R). \tag{2.15}$$

The quantities $\lambda^{j\pm}$ are the maximum and the minimum of the eigenvalues in the Jacobian matrix of the flux vectors as

$$\lambda^{j\pm} = v^j \pm c_s, \tag{2.16}$$

where c_s is a speed of sound.

We check the ability of our new HLL flux scheme to resolve shocks by solving a wall shock problem, in which two phases of a fluid collide at supersonic speeds. In Fig. 1, we compare numerical results with the analytic solutions for initial velocities that are similar to those found in our simulations in Sec. IV. We find good agreement for Mach numbers up to $M_{\rm mach} \lesssim 7$, which is a typical number in our simulations.

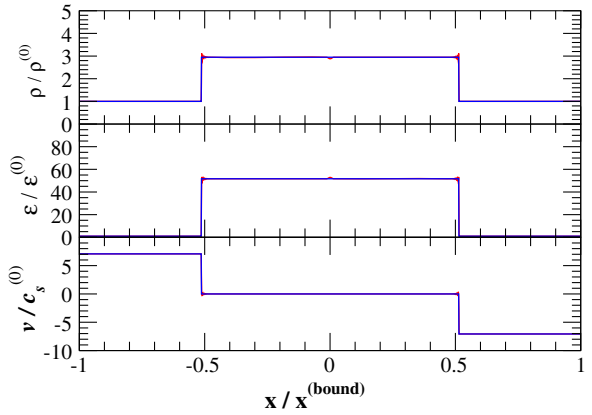

FIG. 1. Comparison of a rest mass density, specific internal energy, and velocity between numerical and analytical results of the one-dimensional wall shock problem at $t = 1.0x^{(\rm bound)}/v_0$. Red and blue lines represent our computational and analytical results. We choose the parameter sets as $\Gamma = 2$, $\kappa_s = 1$ with grid space $\Delta x = 1.0 \times 10^{-3} x^{(\rm bound)}$ and $v_0 = 7.07 c_s^{(0)}$, where $c_s^{(0)}$ is the initial speed of sound at $t = 0$.

III. LINEAR PERTURBATION

A. Basic equations in a nonaxisymmetric perturbation

We perturb the differentially rotating stars nonaxisymmetrically in order to investigate the feature of low T/W dynamical instabilities. We assume a harmonic dependence of time and azimuthal angle on the perturbed quantity δq as

$$\delta q(t, \varpi, z, \varphi) = \sum_m \delta q_m(\varpi, z) e^{-i\omega t + im\varphi}, \tag{3.1}$$

where z is the coordinate along the rotational axis, φ the azimuthal coordinate, and m the azimuthal wave number. The perturbed Euler equations can be written as [31]

$$Q^{-1}_{ij}\delta v^j \equiv [i\tilde{\omega}\gamma_{ij} - 2\nabla_j v_i + \phi_i \nabla_j \Omega]\delta v^j = \nabla_i \delta U, \tag{3.2}$$

where δv^i is the perturbed velocity, v^i the equilibrium distribution of the velocity, $\tilde{\omega} = \omega - m\Omega$, γ_{ij} the spatial 3-metric, ϕ^i the rotational Killing vector, δU the scalar potential $\delta U \equiv \delta h + \delta\Phi$, δh the perturbed enthalpy, and $\delta\Phi$ the perturbed gravitational potential. Note that we define the tensorial quantity Q_{ij} in Eq. (3.2).

Assuming a barotropic relation $p = p(\rho)$ in the equation of state, a perturbed rest mass density $\delta\rho$ can be written as

$$\delta\rho = \rho \frac{d\rho}{dp}\delta h = \rho \frac{d\rho}{dp}(\delta U - \delta\Phi). \tag{3.3}$$

Using Eq. (3.3), the conservation equation of the perturbed rest mass is described using δU and $\delta\Phi$ as

$$-i\tilde{\omega}\rho\frac{d\rho}{dp}(\delta U - \delta\Phi) + \nabla_i(\rho Q^{ij}\nabla_j \delta U) = 0. \tag{3.4}$$

Combining Eqs. (3.2) and (3.4), one of the pulsation equations of rotating stars becomes second-order partially differential equations as

$$\left[\frac{\partial^2}{\partial\varpi^2} - \left(\frac{\partial}{\partial\varpi}\ln\frac{D}{\rho\varpi}\right)\frac{\partial}{\partial\varpi} - \frac{2m\Omega}{\varpi\tilde{\omega}}\left(\frac{\partial}{\partial\varpi}\ln\frac{\rho\Omega}{D}\right) - \frac{m^2}{\varpi^2} - \frac{D}{\tilde{\omega}^2}\left(\frac{\partial^2}{\partial z^2} + \frac{1}{\rho}\frac{\partial\rho}{\partial z}\frac{\partial}{\partial z}\right) - \frac{D}{dp/d\rho}\right]\delta U_m(\varpi, z) = -\frac{D}{dp/d\rho}\delta\Phi_m(\varpi, z), \tag{3.5}$$

where $D = \kappa^2 - \tilde{\omega}^2$ and κ^2 is $\varpi(d\Omega^2/d\varpi) + 4\Omega^2$. The perturbed Poisson's equation is

$$\nabla_j\nabla^j\delta\Phi = 4\pi\rho\frac{d\rho}{dp}(\delta U - \delta\Phi), \tag{3.6}$$

and it is explicitly expressed as

$$\left[\frac{\partial^2}{\partial\varpi^2}+\frac{1}{\varpi}\frac{\partial}{\partial\varpi}-\frac{m^2}{\varpi^2}+\frac{\partial^2}{\partial z^2}+4\pi\rho\frac{d\rho}{dp}\right]\delta\Phi_m(\varpi,z) = 4\pi\rho\frac{d\rho}{dp}\delta U_m(\varpi,z). \tag{3.7}$$

To conclude, the basic pulsation equations of δU_m and $\delta\Phi_m$ are Eqs. (3.5) and (3.7).

B. Cylindrical model

We impose one assumption in which the equatorial motion of the perturbed quantities of the stars alone is taken into account. Our basic idea is that a characteristic wave propagation mainly lies in the equatorial plane in a rotating configuration. Therefore, we simply discard the second-order z derivatives in δU_m and $\delta\Phi_m$ (the first-order z derivatives in δU_m and $\delta\Phi_m$ automatically disappear due to an equatorial symmetry which we imposed in the system). We call this system a cylindrical model.

The basic equations [Eqs. (3.5) and (3.7)] in the cylindrical model become (see, e.g., [24,32])

$$\left[\frac{d^2}{d\varpi^2}-\left(\frac{d}{d\varpi}\ln\frac{D}{\rho\varpi}\right)\frac{d}{d\varpi}-\frac{2m\Omega}{\varpi\tilde{\omega}}\left(\frac{d}{d\varpi}\ln\frac{\rho\Omega}{D}\right)-\frac{m^2}{\varpi^2}-\frac{D}{dp/d\rho}\right]\delta U_m(\varpi) = -\frac{D}{dp/d\rho}\delta\Phi_m(\varpi), \tag{3.8}$$

$$\left[\frac{d^2}{d\varpi^2}+\frac{1}{\varpi}\frac{d}{d\varpi}-\frac{m^2}{\varpi^2}+4\pi\rho\frac{d\rho}{dp}\right]\delta\Phi_m(\varpi) = 4\pi\rho\frac{d\rho}{dp}\delta U_m(\varpi). \tag{3.9}$$

We introduce an eigenvalue problem for studying the stability of the system. We impose regularity conditions at the center for δU_m and $\delta\Phi_m$ as

$$\delta U_m = C_m^1\varpi^{|m|}, \qquad \delta\Phi_m = C_m^2\varpi^{|m|}, \tag{3.10}$$

where C_m^1 and C_m^2 are constants. We also impose a boundary condition for a perturbed gravitational potential $\delta\Phi_m$ at infinity as the quantity is finite ($\delta\Phi_m \propto \varpi^{-|m|}$). That is to say, we can equivalently impose a boundary condition on the surface as

$$\delta\Phi_m = C_m^3\varpi^{-|m|}, \tag{3.11}$$

in our model. Using the nature of linear perturbation, the constant C_m^3 is described as an appropriate combination of C_m^1 and C_m^2, which is determined from the condition that $\delta\Phi_m$ and $d\delta\Phi_m/d\varpi$ are continuous across the surface. In practice, we can construct two sets of solutions ($\delta U_m^{(1)}$, $\delta\Phi_m^{(1)}$) and ($\delta U_m^{(2)}$, $\delta\Phi_m^{(2)}$) by integrating Eqs. (3.8) and (3.9), keeping the same C_m^1 but different C_m^2 ($C_m^{2(1)}$ and $C_m^{2(2)}$) from the center to the surface. Although these solutions do not satisfy the boundary condition on the surface [Eq. (3.11)] in general, we are able to construct a solution by linearly combining these two sets of solutions as

$$\delta U_m = p_m^{(1)}\delta U_m^{(1)} + p_m^{(2)}\delta U_m^{(2)}, \tag{3.12}$$

$$\delta\Phi_m = p_m^{(1)}\delta\Phi_m^{(1)} + p_m^{(2)}\delta\Phi_m^{(2)}, \tag{3.13}$$

where $p_m^{(1)}$ and $p_m^{(2)}$ should satisfy

$$p_m^{(1)}\left(\delta\Phi_m^{(1)}|_{\varpi=r_e}+\frac{r_e}{m}\left.\frac{d\Phi_m^{(1)}}{d\varpi}\right|_{\varpi=r_e}\right) + p_m^{(2)}\left(\delta\Phi_m^{(2)}|_{\varpi=r_e}+\frac{r_e}{m}\left.\frac{d\Phi_m^{(2)}}{d\varpi}\right|_{\varpi=r_e}\right) = 0, \tag{3.14}$$

to meet the surface boundary condition for $\delta\Phi_m$ [Eq. (3.11)]. Note that r_e represents the equatorial radius of the star. The constant C_m^3 can then be written by using $p_m^{(1)}$ and $p_m^{(2)}$ as

$$C_m^3 = r_e^{|m|}(p_m^{(1)}\delta\Phi_m^{(1)}|_{\varpi=r_e} + p_m^{(2)}\delta\Phi_m^{(2)}|_{\varpi=r_e}), \tag{3.15}$$

remaining as one scaling freedom.

We also impose a surface boundary condition for δU_m as the enthalpy vanishes on the oscillating surface. Namely

$$\delta h_m + \xi_m^j\nabla_j h = 0, \tag{3.16}$$

where h is the equilibrium enthalpy, ξ_m^i is the Lagrangian displacement [33] of the m mode as

$$\xi_{mi} = i\left[\frac{\gamma_{ij}}{\tilde{\omega}}+i\frac{\phi_i\nabla_j\Omega}{\tilde{\omega}^2}\right]\delta v_m^j, \tag{3.17}$$

and δv_m^i is the perturbed velocity of the m mode. A concrete boundary condition for δU_m along the equatorial plane in the cylindrical coordinates is written as

$$\delta U_m - \delta\Phi_m - \frac{1}{D}(\nabla_\varpi\delta U_m)(\nabla_\varpi U - \nabla_\varpi\Phi) + \frac{2m\Omega}{\varpi\tilde{\omega}D}(\nabla_\varpi U - \nabla_\varpi\Phi)\delta U_m = 0. \tag{3.18}$$

Note that we impose a planner symmetry across the equatorial plane for an equilibrium configuration to derive Eq. (3.18). We also apply the Euler equations [Eq. (2.6)] to compute the term $\nabla_\varpi U - \nabla_\varpi\Phi$ on the boundary as

$$\nabla_\varpi U - \nabla_\varpi\Phi = -\nabla_\varpi\Phi + \varpi\Omega^2. \tag{3.19}$$

Only 1 degree of freedom remains in the system, which represents the normalization factor in linear perturbation. We set $C^1_m = 1$ in our computational code, closing the system as an eigenvalue problem.

C. Spheroidal model

Here we introduce a spheroidal model to take a stellar configuration partially into account. Instead of discarding z derivative in the basic equation of δU_m in the cylindrical model, we assume a solution for the polar direction θ in the spherical coordinates as Legendre polynomial $P^m_l(\cos\theta)$,

$$\delta U = \sum_{l,m} \delta U_{lm}(r) P^m_l(\cos\theta) e^{-i\omega t + im\varphi}, \tag{3.20}$$

$$\delta \Phi = \sum_{l,m} \delta \Phi_{lm}(r) P^m_l(\cos\theta) e^{-i\omega t + im\varphi}. \tag{3.21}$$

The basic equations in the spheroidal model are written as (see, e.g., [33])

$$\begin{aligned}
&\left[\frac{d^2}{dr^2} + \left[\frac{1}{r}\left(2 - \frac{\kappa^2}{\tilde\omega^2}\right) + \frac{1}{\rho}\frac{d\rho}{dr} - \frac{1}{D}\frac{\partial D}{d\varpi}\right]\frac{d}{dr}\right.\\
&\quad - \frac{2m\Omega}{r\tilde\omega}\left(\frac{1}{\rho}\frac{d\rho}{dr} + \frac{1}{\Omega}\frac{d\Omega}{d\varpi} - \frac{1}{D}\frac{dD}{d\varpi}\right) - \frac{D}{dp/d\rho}\\
&\quad \left. - \frac{1}{r^2}\left[m^2 + \left(1 - \frac{\kappa^2}{\tilde\omega^2}\right)[l(l+1) - m^2]\right]\right]\delta U_{lm}(r)\\
&= -\frac{D}{dp/d\rho}\delta\Phi_{lm}(r),
\end{aligned} \tag{3.22}$$

$$\begin{aligned}
&\left[\frac{d^2}{dr^2} + \frac{2}{r}\frac{d}{dr} - \frac{l(l+1)}{r^2} + 4\pi\rho\frac{d\rho}{dp}\right]\delta\Phi_{lm}(r)\\
&\quad = 4\pi\rho\frac{d\rho}{dp}\delta U_{lm}(r).
\end{aligned} \tag{3.23}$$

The boundary condition can be imposed in the same manner as that in the cylindrical model. We explain the derivation of a boundary condition at the center in Appendix. In summary, the regularity condition at the center can be written as

$$\delta U_{lm} = C^1_{lm} r^{\max(\Re[\lambda^{(1)}_{lm}], \Re[\lambda^{(2)}_{lm}])}, \qquad \delta\Phi_{lm} = C^2_{lm} r^l,$$

where $\lambda^{(1)}_{lm}$ and $\lambda^{(2)}_{lm}$ are the solutions of Eq. (A5), and C^1_{lm} and C^2_{lm} are constants. A surface boundary condition is given as $\delta\Phi_{lm} = C^3_{lm} r^{-(l+1)}$, where C^3_{lm} is a function of C^1_{lm} and C^2_{lm} (enable to apply the same technique to meet the surface boundary condition as in the cylindrical model), and the condition for δU_{lm} is

$$\delta h_{lm} + \xi^j_{lm}\nabla_j h = 0, \tag{3.24}$$

on the surface. We write down a concrete boundary condition along the equatorial plane in spherical coordinates as

$$\begin{aligned}
&\delta U_{lm} - \delta\Phi_{lm} - \frac{1}{D}(\nabla_r \delta U_{lm})(\nabla_r U - \nabla_r \Phi)\\
&\quad + \frac{2m\Omega}{\varpi\tilde\omega D}(\nabla_r U - \nabla_r\Phi)\delta U_{lm} = 0,
\end{aligned}$$

imposing a planner symmetry across the equatorial plane for an equilibrium configuration. In conclusion, the system is also set as an eigenvalue problem.

D. Reflection waves

In Secs. III B and III C, we formulate the stability analysis by finding complex eigenmodes. Here we introduce another approach to study the stability of the system: a wave amplification by inserting incoming waves from the surface to corotation. Although the basic idea has already been given in Ref. [25], here we write down our techniques, which are useful for computing large parameter sets and comparing the results with those of numerical simulations. We rewrite the basic equation of the scalar potential δU_m [Eq. (3.8)] to focus on the nature of a wave propagation as [32]

$$\left[\frac{d^2}{d\varpi^2} - V^{\rm eff}_m(\varpi)\right]\delta\eta_m(\varpi) = -\frac{D}{dp/d\rho}S^{-1/2}\delta\Phi_m(\varpi), \tag{3.25}$$

where

$$\begin{aligned}
S &\equiv \frac{D}{\rho\varpi}, \qquad \delta\eta_m \equiv S^{-1/2}\delta U_m,\\
V^{\rm eff}_m(\varpi) &\equiv \frac{D}{dp/d\rho} + \frac{m^2}{\varpi^2} + \frac{2m\Omega}{\varpi\tilde\omega}\left(\frac{d}{d\varpi}\ln\frac{\rho\Omega}{D}\right)\\
&\quad - S^{1/2}\frac{d^2}{d^2\varpi}S^{-1/2}.
\end{aligned}$$

Note that the quantity $V^{\rm eff}_m$ is regarded as an effective potential of the wave propagation and contains the $\tilde\omega^{-1}$ term. Although it is useful to introduce an effective potential to understand the mechanism of a corotation amplification, the solution $\delta\eta_m$ contains an apparent singular behavior at Lindbald radius (the radius where $D = 0$). Therefore, we first construct the solution of Eq. (3.25) using a scalar potential δU_m, which does not contain a singular behavior at Lindbald radius, and then transfer the scalar potential δU_m to the perturbed quantity $\delta\eta_m$ to avoid the apparent singular behavior.

The basic equation around corotation ($\tilde\omega \approx 0$) can be expressed by extracting the dominant contribution to the singular behavior in the effective potential $V^{\rm eff}_m$ as

$$\left[\frac{d^2}{d^2\varpi}-\frac{2m\Omega}{\varpi\tilde{\omega}}\left(\frac{d}{d\varpi}\ln\frac{\rho\Omega}{D}\right)\right]\delta U_m(\varpi)=0. \tag{3.26}$$

The quantity $\tilde{\omega}$ can be expanded up to the first order of $\varpi-\varpi_{\rm cr}$ as

$$\begin{aligned}\tilde{\omega}&=\Re[\omega]+i\Im[\omega]-m\Omega\\&=-m\frac{d\Omega}{d\varpi}\bigg|_{\varpi=\varpi_{\rm cr}}(\varpi-\varpi_{\rm cr})+i\Im[\omega]\\&=\frac{g_{\rm cr}\Re[\omega]}{\varpi_{\rm cr}}(\varpi-\Pi_{\rm cr}),\end{aligned}$$

where $\varpi_{\rm cr}$ is the cylindrical radius at corotation, $g_{\rm cr}\equiv-(\varpi_{\rm cr}/\Omega_{\rm cr})(d\Omega/d\varpi)_{\varpi=\varpi_{\rm cr}}$, and $\Pi_{\rm cr}\equiv\varpi_{\rm cr}-i(\varpi_{\rm cr}\Im[\omega])/(g_{\rm cr}\Re[\omega])$. Then, Eq. (3.26) can be written as

$$\left[\frac{d^2}{d^2w}+\frac{\beta_{\rm cr}}{w}\right]\delta U_m(w)=0, \tag{3.27}$$

where

$$w=\varpi-\varpi_{\rm cr}+i\frac{\varpi_{\rm cr}\Im[\omega]}{g\Re[\omega]}, \tag{3.28}$$

$$\beta_{\rm cr}\equiv\frac{2}{g_{\rm cr}}\frac{d}{d\varpi}\ln\frac{\kappa^2}{\rho\Omega}\bigg|_{\varpi=\varpi_{\rm cr}}, \tag{3.29}$$

introducing a complex coordinate w in a replacement of a radial one ϖ. To construct a solution δU_m around corotation analytically, we perform a coordinate transformation as $w=s^2$. The basic equation can then be written as

$$\left[\frac{d^2}{ds^2}+\frac{1}{s}\frac{d}{ds}+\left(4\beta_{\rm cr}-\frac{1}{s^2}\right)\right]\delta\Psi_m(s)=0, \tag{3.30}$$

where $\delta U_m=s\delta\Psi_m$. Another coordinate transformation $s=q/(2i\sqrt{|\beta_{\rm cr}|})$, where $\beta_{\rm cr}<0$ in our equilibrium case, leads to the basic equation of $\nu=1$ Bessel functions as

$$\left[\frac{d^2}{dq^2}+\frac{1}{q}\frac{d}{dq}+\left(1-\frac{1}{q^2}\right)\right]\delta\Psi_m(q)=0, \tag{3.31}$$

containing two independent solutions $N_1(q)$ and $J_1(q)$. The general solutions of δU_m, using Taylor's expansion around corotation, can then be written as

$$\delta U_m(w)=A_m^1 w+A_m^2[-4+w(\ln|w|+2\gamma-2\ln 2-1)], \tag{3.32}$$

where γ is Euler's constant, and A_m^1 and A_m^2 are constants. The term $w\ln|w|$ in Eq. (3.32) is the origin of a singular behavior of δU_m on corotation in a cylindrical model.

Next we explain our bridging techniques around corotation. Since we are focusing on the unstable solution, we introduce a semicircular path in the positive imaginary plane to avoid the corotation singularity in the real axis. In fact, only an argument difference appears when bridging the solution at corotation. Inserting $w=\varepsilon_{\rm cr}e^{i(\varphi-\pi)}$ ($\varepsilon_{\rm cr}$ is the radius and φ the angle) in the general solution, a relation between the solution inside δU_m^- and outside corotation δU_m^+ becomes

$$\delta U_m^-(\varpi)=A_m^1\varpi+A_m^2[-4+\varpi(\ln|\varpi|+2\gamma-2\ln 2-1)]\quad\text{as }\varpi<\varpi_{\rm cr}, \tag{3.33}$$

$$\delta U_m^+(\varpi)=A_m^1\varpi+A_m^2[-4+\varpi(\ln|\varpi|-i\pi+2\gamma-2\ln 2-1)]\quad\text{as }\varpi>\varpi_{\rm cr}. \tag{3.34}$$

We can construct a solution δU_m which contains an incoming and a reflection wave outside corotation as follows. First, we impose a regularity condition at the center for δU_m and $\delta\Phi_m$ [Eq. (3.10)], and we solve a pair of second-order ordinary differential equations [Eqs. (3.8) and (3.9)] up to corotation. Using an analytical bridging technique only for δU_m (computing the two constants A_m^1 and A_m^2 inside corotation from δU_m^- and $d\delta U_m^-/d\varpi$ and construct δU_m^+ and $d\delta U_m^+/d\varpi$ from these constants), we are able to solve continuously a pair of second-order ordinary differential equations [Eqs. (3.8) and (3.9)] from corotation up to the surface. Note that we adopt the same technique to impose a boundary condition for $\delta\Phi_m$ on the surface ($\delta\Phi_m=C_m^3\varpi^{-|m|}$) as in Sec. III B.

After constructing a solution of the perturbed quantity $\delta\eta_m$ from a scalar potential δU_m, here we explain our method to extract the reflection amplitude. The solution of a perturbed quantity $\delta\eta_m$ in the wave propagation region can be explained as

$$\delta\eta_m(\varpi)=I_m(\varpi)e^{-ik_m\varpi}+R_m(\varpi)e^{ik_m\varpi}, \tag{3.35}$$

where $k_m\equiv\sqrt{-V_m^{\rm eff}}$. Using $\delta\eta_m$ and $d\delta\eta_m/d\varpi$ around the surface, an amplitude of incoming and outgoing waves to corotation around the surface can be extracted as

$$I_m(\varpi)=\frac{1}{2}e^{ik_m\varpi}\left(\delta\eta_m-\frac{1}{ik_m}\frac{d\delta\eta_m}{d\varpi}\right), \tag{3.36}$$

$$R_m(\varpi)=\frac{1}{2}e^{-ik_m\varpi}\left(\delta\eta_m+\frac{1}{ik_m}\frac{d\delta\eta_m}{d\varpi}\right). \tag{3.37}$$

The growth timescale can be interpreted as an amplification of sound waves by the corotation barrier through a single reflection cycle of the waves. Suppose a perturbed quantity $\delta\eta_m$ grows exponentially in time in the wave propagation regime as

$$\delta\eta_m(t,\varpi) = e^{-i\omega_{\rm ref}t}(I_m(\varpi)e^{-ik_m\varpi} + R_m(\varpi)e^{ik_m\varpi}) = e^{\Im[\omega_{\rm ref}]t}(I_m(\varpi)e^{-i(\Re[\omega_{\rm ref}]t+k_m\varpi)} + R_m(\varpi)e^{-i(\Re[\omega_{\rm ref}]t-k_m\varpi)}), \quad (3.38)$$

where $\omega_{\rm ref}$ is a complex frequency including a growth timescale in the imaginary part, illustrating a wave amplification due to the corotation barrier. The amplification rate through a single wave reflection by the effective potential is $|R_m|/|I_m|$. Once we introduce a wave-traveling time T_m through one reflection by the potential, a relation between the amplification factor and the imaginary part of the frequency is

$$\frac{|R_m|}{|I_m|} = \exp\left[\Im[\omega_{\rm ref}]T_m\right], \quad (3.39)$$

where the wave-traveling time T_m is computed as

$$T_m = \frac{2}{\Re[\omega_{\rm ref}]}\int_{\varpi_{\rm Vmin}}^{\varpi_{\rm Vmax}} k_m d\varpi. \quad (3.40)$$

Note that the radii $\varpi_{\rm Vmin}$ and $\varpi_{\rm Vmax}$(or the equatorial surface radius r_e if there is no such radius) represent the turning point (the radius where $V_m^{\rm eff} = 0$) outside corotation, and the frequency $\Re[\omega_{\rm ref}]$ is taken from the real part of the eigenfrequency by the normal mode analysis computed in Sec. III B. The imaginary part of the frequency $\Im[\omega_{\rm ref}]$ is derived from Eq. (3.39) as

$$\Im[\omega_{\rm ref}] = \frac{\ln|R_m| - \ln|I_m|}{T_m} = \frac{\Re[\omega_{\rm ref}](\ln|R_m| - \ln|I_m|)}{2\int_{\varpi_{\rm Vmin}}^{\varpi_{\rm Vmax}} k_m d\varpi}, \quad (3.41)$$

extracting the amplitude of inserted and amplified waves at the radius $\varpi = \varpi_{\rm Vmax}$.

E. Stability analysis

The axisymmetric equilibrium configuration of the differentially rotating stars is computed in the two-dimensional cylindrical coordinates [34]. Then we take the equilibrium quantities, the pressure over rest mass density q ($\equiv p/\rho$) and gravitational potential Φ, 3841 grid points uniformly along the equatorial plane from the center to the stellar surface in order to integrate the pulsation equations. We use the fourth-order Runge-Kutta method (fourth-order integration in space) to integrate Eqs. (3.8) and (3.9) for cylindrical models

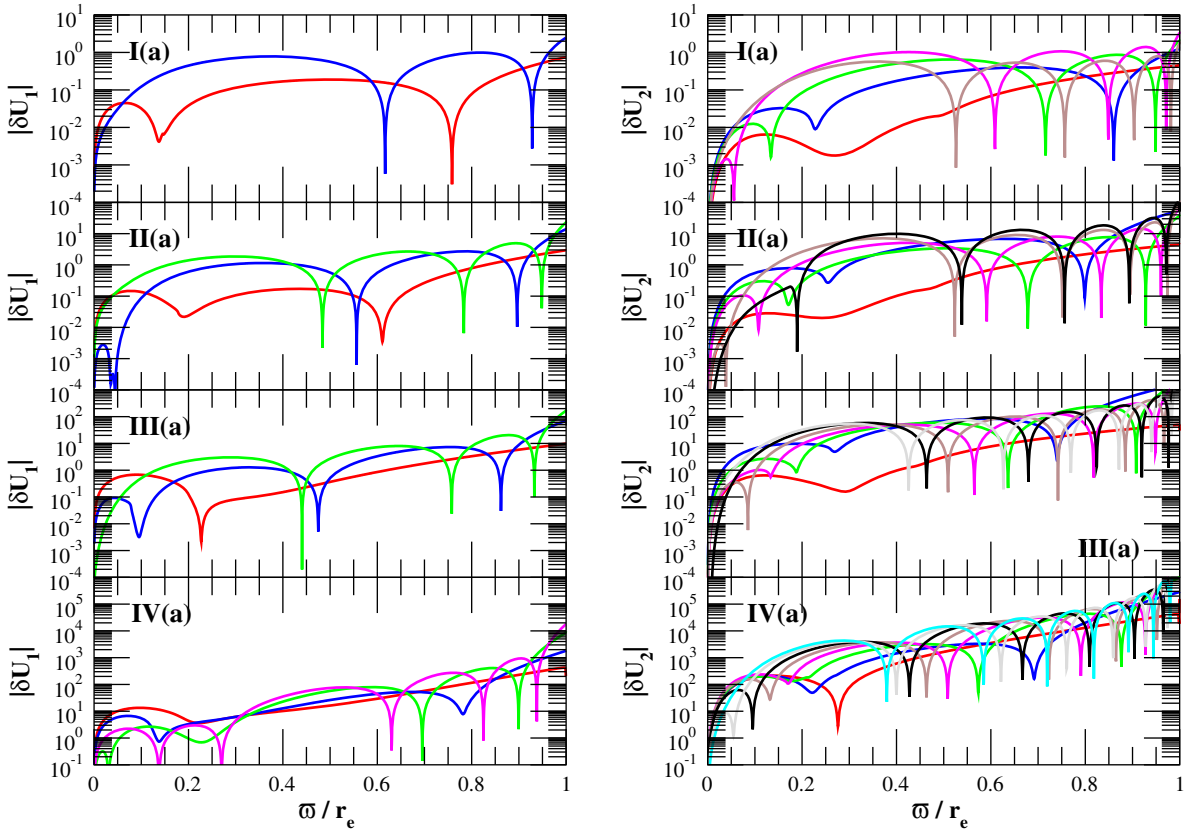

FIG. 2. The $m = 1$ and $m = 2$ eigenfunctions $|\delta U_m|$ for four low T/W dynamically unstable stars in cylindrical models. The labels I (a), II(a), III(a), and IV(a), respectively, represent the equilibrium models in Table I. Red, blue, green, magenta, brown, black, grey, and cyan, respectively, represent the node number between corotation and surface of $N = 0$, 1, 2, 3, 4, 5, 6, and 7. The increasing number of nodes between corotation and the surface can clearly be seen in all eigenfunctions.

and Eqs. (3.22) and (3.23) for spheroidal models with both 1921 grid points in the normal mode analysis.

We search the complex frequency ω in the region of $\Re[\omega] \in [0,4]\Omega_c$ and $\Im[\omega] \in [0,0.2]\Omega_c$, integrating Eqs. (3.8) and (3.9) for cylindrical models or Eqs. (3.22) and (3.23) for spheroidal models from the center to the surface to check whether the boundary condition of Eq. (3.16) for cylindrical models or Eq. (3.24) for spheroidal models is satisfied. Note that the frequency we search covers the region where corotation exists inside the stars. In fact, we compute the left-hand side of Eq. (3.16) for cylindrical models or Eq. (3.24) for spheroidal models normalized by δh_m or δh_{lm} for each complex frequency, and we determine the eigenfrequency once the following two conditions are satisfied. The first is that the relative error of the left-hand side of Eq. (3.16) for cylindrical models or Eq. (3.24) for spheroidal models normalized by δh_m or δh_{lm} is less than 2×10^{-3}. The second is that the frequency takes the minimum around the neighboring four complex frequencies of each grid point in the complex plane. Our frequency resolution for finding the eigenfrequency is $\Delta\omega = 1 \times 10^{-5}$ for both real and imaginary parts. We only focus on $m = 1$ spiral and $m = 2$ bar mode here.

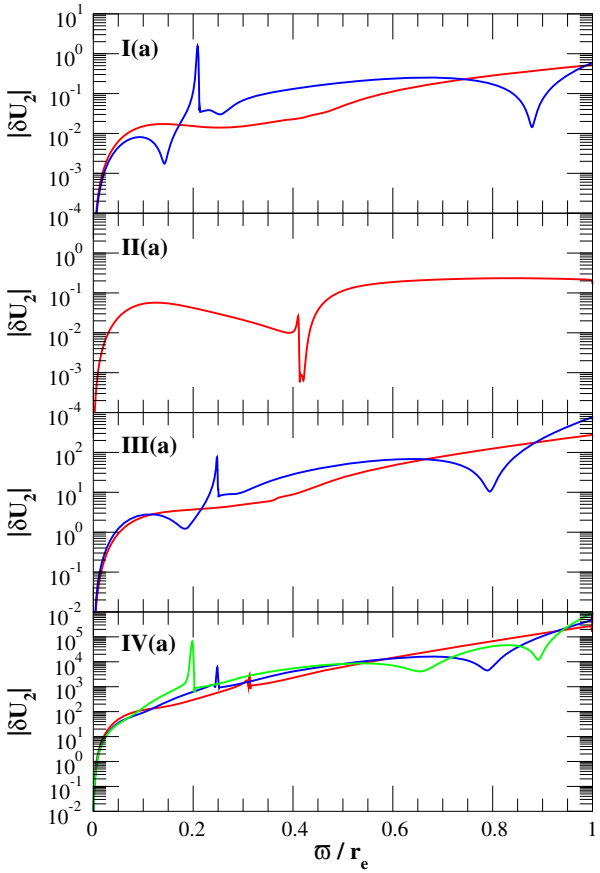

FIG. 3. Same as Fig. 2, but for $m = 2$ eigenfunctions $|\delta U_m|$ in spheroidal models.

We show the eigenfrequencies from the linear perturbation analysis in Tables II–V for cylindrical models and in Table VI for spheroidal models. We also show the eigenfunctions in Fig. 2 for cylindrical models and in Fig. 3 for spheroidal models. As we have already stated in Ref. [24], we find the following three conclusions. One is that an oscillation between corotation and the surface can be found in all eigenfunctions. Every node number can be seen in all differentially rotating stars for the $m = 2$ bar mode. Note that some of the zero nodes for $m = 1$, which represents the shift of the center of mass, correspond to the pure imaginary eigenfrequency (we omit these pure imaginary eigenfrequencies from the tables). Another is that all eigenfrequencies that have a corotation inside the star are unstable (existence of a positive imaginary part in eigenfrequencies). This fact indicates that the existence of corotation triggers dynamical instabilities. The other is that $m = 1$ dynamical instabilities become dominant in a soft equation of state. This means that we are able to identify the stiffness of the equation of state by the direct detection of gravitational waves.

For the reflection wave analysis, we basically adopt the same computational technique as in the normal mode analysis. We take again the equilibrium quantities, the pressure over rest mass density q and gravitational potential

TABLE II. The $m = 1$ and $m = 2$ normal modes of $n = 1$ differentially rotating stars in the cylindrical model.

Model	m	N[a]	$\Re[\omega]/\Omega_c$	$\Im[\omega]/\Omega_c$	$r_{\rm cr}/r_e$[b]	$\Im[\omega]_{\rm ref}/\Omega_c$[c]
I(a)	1	1	0.65275	0.00012	0.14587	0.00001
I(a)	1	2	1.15197	0.00000	···	···
I(a)	2	0	0.29017	0.00855	0.48549	0.00110
I(a)	2	1	0.89791	0.00100	0.22158	0.00005
I(a)	2	2	1.39597	0.00039	0.13156	0.00001
I(a)	2	3	1.86074	0.00024	0.05471	0.00000
I(a)	2	4	2.31080	0.00000	···	···
I(b)	1	1	0.53732	0.00001	0.27838	0.00000
I(b)	1	2	1.77131	0.00000	···	···
I(b)	2	0	0.42797	0.01568	0.57497	0.00122
I(b)	2	1	1.40812	0.00036	0.19450	0.00001
I(b)	2	2	2.17266	0.00000	···	···
I(c)	1	0	1.20707	0.00000	···	···
I(c)	2	0	0.56668	0.00001	0.79519	NA[d]
I(c)	2	1	2.31692	0.00000	···	···
I(d)	1	0	2.23106	0.00000	···	···
I(d)	2	0	0.70460	0.22153	···	···
I(d)	2	1	3.66914	0.00000	···	···

[a] N: Node numbers between corotation and equatorial surface radius.
[b] $r_{\rm cr}$: Corotation radius.
[c] $\Im[\omega]_{\rm ref}$: Imaginary part of the complex frequency computed from the amplification timescale.
[d] NA: No amplification.

TABLE III. Same as Table II, but of $n = 1.5$ differentially rotating stars.

Model	m	N	$\Re[\omega]/\Omega_c$	$\Im[\omega]/\Omega_c$	$r_{\rm cr}/r_e$	$\Im[\omega]_{\rm ref}/\Omega_c$
II(a)	1	1	0.55723	0.00080	0.17828	0.00016
II(a)	1	2	0.97454	0.00019	0.03233	0.00000
II(a)	1	3	1.34786	0.00000	···	···
II(a)	2	0	0.31734	0.00841	0.46054	0.00001
II(a)	2	1	0.78994	0.00196	0.24753	0.00007
II(a)	2	2	1.18978	0.00026	0.16504	0.00037
II(a)	2	3	1.56573	0.00044	0.10533	0.00008
II(a)	2	4	1.92897	0.00001	0.03838	0.00000
II(a)	2	5	2.00084	0.00000	···	···
II(b)	1	1	0.53737	0.00001	0.27836	NA
II(b)	1	2	1.48459	0.00000	···	···
II(b)	2	0	0.44482	0.00723	0.56094	0.00003
II(b)	2	1	1.22913	0.00024	0.23758	0.00147
II(b)	2	2	1.83866	0.00042	0.08887	0.00001
II(b)	2	3	2.00188	0.00000	···	···
II(c)	1	0	1.20707	0.00000	···	···
II(c)	2	0	0.58081	0.00001	0.78158	0.00332
II(c)	2	1	1.70706	0.00001	0.20713	0.00031
II(c)	2	2	2.00116	0.00000	···	···
II(d)	1	0	2.17560	0.00000	···	···
II(d)	2	0	0.31532	0.00000	···	···
II(d)	2	1	1.17702	0.00001	0.83619	NA
II(d)	2	2	3.03110	0.00000	···	···

TABLE IV. Same as Table II, but of $n = 2$ differentially rotating stars.

Model	m	N	$\Re[\omega]/\Omega_c$	$\Im[\omega]/\Omega_c$	$r_{\rm cr}/r_e$	$\Im[\omega]_{\rm ref}/\Omega_c$
III(a)	1	1	0.50040	0.00553	0.19984	0.00053
III(a)	1	2	0.86641	0.00018	0.07853	0.00001
III(a)	1	3	1.18793	0.00000	···	···
III(a)	2	0	0.35218	0.00676	0.43262	0.00012
III(a)	2	1	0.73570	0.00249	0.26218	0.00056
III(a)	2	2	1.06871	0.00027	0.18670	NA
III(a)	2	3	1.38662	0.00001	0.13302	0.00001
III(a)	2	4	1.69457	0.00001	0.08491	0.00000
III(a)	2	5	1.99668	0.00001	0.00816	NA
III(a)	2	6	2.29444	0.00000	···	···
III(b)	1	1	0.74278	0.00635	0.17654	0.00015
III(b)	1	3	1.30342	0.00000	···	···
III(b)	2	0	0.47957	0.00006	0.53417	0.00639
III(b)	2	1	1.13383	0.00024	0.26221	0.00002
III(b)	2	2	1.63501	0.00040	0.14174	0.00000
III(b)	2	3	2.10710	0.00000	···	···
III(c)	1	0	1.20716	0.00000	···	···
III(c)	2	0	0.81573	0.00002	0.60245	NA
III(c)	2	1	1.82914	0.00027	0.15282	0.00002
III(c)	2	2	2.56178	0.00000	···	···
III(d)	1	0	2.14064	0.00000	···	···
III(d)	2	0	0.16891	0.00000	···	···
III(d)	2	1	2.23895	0.00000	···	···

Φ, 3841 grid points uniformly along the equatorial plane, and use the fourth-order Runge-Kutta method (fourth-order integration in space) to integrate Eqs. (3.8) and (3.9) for cylindrical models with both 1921 grid points in the normal mode analysis. Only the difference of computational techniques from the normal mode analysis is an introduction of bridging of the perturbed scalar potential δU_m around corotation due to a coordinate singularity at corotation. We assume that the corotation is not located on the grid point (the measure is zero in a mathematical sense), and we separate two regions as inside and outside corotation. Bridging the perturbed scalar function δU_m between two different regions, two constants A^1_m and A^2_m at the closest inner grid point to corotation are used to construct the solution. We summarize our finding of the reflection timescale (corresponds to an imaginary part of the reflection frequency), which is based on the idea of an amplification mechanism through a corotation singularity, in Tables II–V for cylindrical models. Although estimating the timescale of a single reflection wave contains many crude approximations (assumption of a wave propagation in the equatorial plane, a transmitting wave is not taken into account for deriving timescale T_m and estimating wave-traveling time is assumed by the time of one reflection from the potential), qualitative features seem to be similar to those of the normal mode analysis. Although a complete understanding of the mechanism requires a two-dimensional nonaxisymmetric perturbation analysis, which is out of our scope in this paper, our finding may enlighten a direction to understand a physical mechanism for low T/W dynamical instabilities.

F. Picture of low T/W dynamical instabilities

In Sec. III D, we qualitatively have good agreement between the stability analysis of a scattering problem and a normal mode analysis. We are able to propose the following mechanism for generating low T/W dynamical instabilities. Suppose that an eigenfrequency of a pulsation mode, such as f or p mode, shows an existence of corotation inside the star. The mode grows exponentially in a nonaxisymmetric manner due to an amplification mechanism. After the angular momentum transport efficiently plays a role due to nonaxisymmetric deformation, the amplification condition may no longer be satisfied. As a result, the growth of the instabilities are at least saturated. If this picture is correct, all existing pulsation modes are the potential candidates to unstabilize the system when the amplification condition sets in. However, the eigenfrequencies that contain corotation inside the star are quite limited

TABLE V. Same as Table II, but of $n = 3$ differentially rotating stars.

Model	m	N	$\Re[\omega]/\Omega_c$	$\Im[\omega]/\Omega_c$	$r_{\rm cr}/r_e$	$\Im[\omega]_{\rm ref}/\Omega_c$
IV(a)	1	0	0.52603	0.05126	0.18985	0.00090
IV(a)	1	1	0.72759	0.00688	0.12238	0.00013
IV(a)	1	2	0.97965	0.00011	0.02883	0.00000
IV(a)	1	3	1.24636	0.00000	···	···
IV(a)	2	0	0.52656	0.00041	0.33456	0.00014
IV(a)	2	1	0.71208	0.00147	0.26897	0.00007
IV(a)	2	2	0.94196	0.00072	0.21197	0.00000
IV(a)	2	3	1.17403	0.00039	0.16775	0.00001
IV(a)	2	4	1.40432	0.00037	0.13026	0.00000
IV(a)	2	5	1.63112	0.00038	0.09511	NA
IV(a)	2	6	1.85820	0.00046	0.05525	0.00000
IV(a)	2	7	2.08739	0.00000	···	···
IV(b)	1	0	0.80474	0.00005	0.14777	0.00058
IV(b)	1	1	1.10578	0.00000	···	···
IV(b)	2	0	0.80198	0.00001	0.36667	0.00018
IV(b)	2	1	1.10851	0.00013	0.26904	0.00019
IV(b)	2	2	1.42299	0.00026	0.19103	0.00001
IV(b)	2	3	1.74841	0.00051	0.11380	NA
IV(b)	2	4	2.07242	0.00000	···	···
IV(c)	1	1	1.20713	0.00000	···	···
IV(c)	2	1	1.70729	0.00001	0.20703	0.00000
IV(c)	2	2	2.30367	0.00000	···	···
IV(d)	1	1	1.47885	0.00000	···	···
IV(d)	2	1	0.16891	0.00000	···	···
IV(d)	2	2	3.56353	0.00000	···	···

in rotating equilibrium stars. Also, a certain degree of differential rotation is required. In addition, the growth timescale depends on the configuration of an effective potential, which is normally powerful to the f mode. Finally, a saturation amplitude depends on the efficiency of the angular momentum transport in the instabilities.

IV. NUMERICAL RESULTS

A. Validity of cylindrical and spheroidal models

We briefly introduce our results of three-dimensional hydrodynamical simulations in Newtonian gravity and compare them with those of linear perturbative analyses. Here we choose three differentially rotating equilibrium stars, keeping the same polytropic index $n = 1$ and degree of differential rotation $\Omega_e/\Omega_c = 26.0$, where Ω_c is the central angular velocity of the star and Ω_e the equatorial surface angular velocity, but varying the deformation rate $1 - r_p/r_e$ as 0.125,0.250,0.375, where r_p is the polar surface radius of the star, summarized in Table VIII. We impose a nonaxisymmetric perturbation in the rest mass density as

TABLE VI. The $m = 2$ normal modes of differentially rotating stars in the spheroidal model.

Model	n	m	N	$\Re[\omega]/\Omega_c$	$\Im[\omega]/\Omega_c$	$r_{\rm cr}/r_e$
I(a)	1	2	0	0.35170	0.01684	0.43297
I(a)	1	2	1	0.93223	0.02054	0.21405
I(b)	1	2	0	0.54951	0.00635	0.48741
I(c)	1	2	0	0.91189	0.06664	0.54618
I(d)	1	2	0	···	···	···
II(a)	1.5	2	0	0.37904	0.00381	0.41359
II(b)	1.5	2	0	0.53495	0.00586	0.49516
II(c)	1.5	2	0	···	···	···
II(d)	1.5	2	0	···	···	···
III(a)	2	2	0	0.44143	0.01844	0.37580
III(a)	2	2	1	0.77193	0.01448	0.25199
III(b)	2	2	0	0.68370	0.03313	0.41626
III(c)	2	2	0	···	···	···
III(d)	2	2	0	···	···	···
IV(a)	3	2	0	0.57186	0.00839	0.31606
IV(a)	3	2	1	0.76898	0.01460	0.25305
IV(a)	3	2	2	0.98177	0.02302	0.20368
IV(b)	3	2	0	0.87934	0.01566	0.33867
IV(c)	3	2	0	···	···	···
IV(d)	3	2	0	···	···	···

$$\rho = \rho_{\rm eq}\left(1 + \delta\frac{x^2 + 2xy - y^2}{r_e^2}\right),$$

where we set $\delta = 5 \times 10^{-3}$ for evolution. Note that $\rho_{\rm eq}$ is an equilibrium configuration of the rest mass density, and x and y are the components of Cartesian coordinates. Note that 161 grid points are covered along the equatorial diameter of the star, with twice the equatorial radius as large as the outer boundary for each coordinate direction. We monitor the diagnostics M_2 as

$$M_m = \langle e^{im\varphi}\rangle_m = \frac{1}{M}\int dv\rho e^{im\varphi}, \tag{4.1}$$

which is $m = 2$ rest mass density weighted average in the whole volume, and find that M_2 grows exponentially for the low T/W dynamically unstable case (Fig. 4). In practice, the M_2 grows exponentially up to $t \approx 50\ P_c$ for models I-i (a) and I-ii(a), and to $t \approx 150\ P_c$ for model I-i(c), and saturates its amplitude around $M_2 \approx 0.1$ for models I-i(a) and II-i(a), and around $M_2 \approx 0.04$ for model III-i(a). We extract the characteristic frequencies in the diagnostics from computing their spectra in Fig. 5 as

$$|F_m|^2 = \left|\frac{1}{M}\int dt\int dx^3\rho e^{i(\omega t - m\varphi)}\right|^2. \tag{4.2}$$

The peak frequencies for models I-i(a), I-ii(a), and I-iii(a) are, respectively, $\omega/\Omega_c = 0.380$, 0.458, and 0.622. Each model contains a single peak in the positive frequency region, indicating that our three models contain one

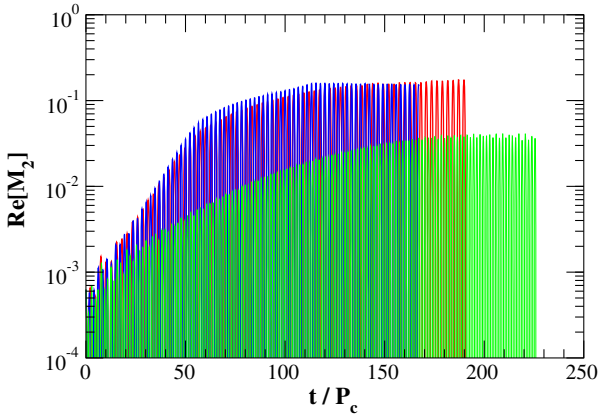

FIG. 4. The M_2 diagnostics for three low T/W $n=1$ dynamically unstable stars. Red, blue, and green lines, respectively, represent models I-i(a), I-ii(a), and I-iii(a). We find an amplified oscillation in the diagnostics for all three cases.

dominant unstable "mode." The growth time of the diagnostics (Fig. 6) is extracted by using a fitting formula of the exponential growth function as

$$M_m = A_m \exp\,[B_m t/P_c], \tag{4.3}$$

where A_m and B_m are the two dimensionless parameters to be fitted for each model. We show a clear fitting to the diagnostics curve in Fig. 6 with the choice of parameter sets described in the caption. The imaginary parts of the characteristic frequencies are extracted by using the relation $\Im[\omega] = B_m/(2\pi)$ as $\Im[\omega]/\Omega_c = 0.0124$ for model I-i(a), 0.0133 for model I-ii(a), and 0.00668 for model I-iii(a).

We also monitor a scalar potential U_m in the simulation [24], which represents the eigenfunction of rotating pulsating stars in Newtonian gravity, as

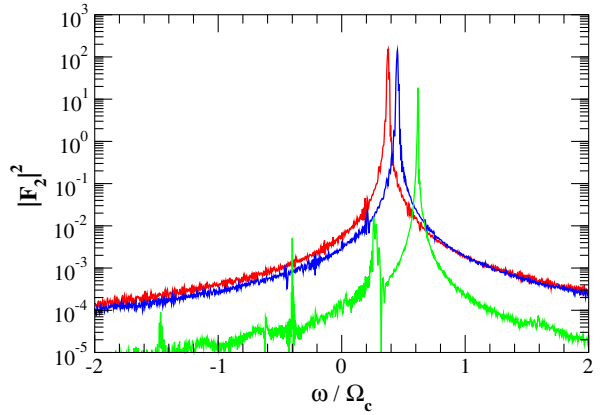

FIG. 5. Spectra of M_2 diagnostics ($|F_2|^2$) for three low T/W $n=1$ dynamically unstable stars. Red, blue, and green lines, respectively, represent models I-i(a), I-ii(a), and I-iii(a). Only a single dominant peak in the spectrum shows that the unstable stars contain one dominant characteristic frequency.

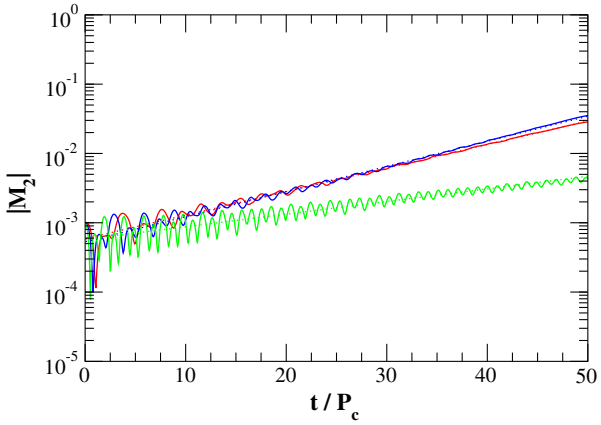

FIG. 6. Growth rate of $|M_2|$ diagnostics for three low T/W $n=1$ dynamically unstable stars. Red, blue, and green lines, respectively, represent models I-i(a), I-ii(a), and I-iii(a). Dotted lines, respectively, represent the fitting formula $|M_2| = A_2 \exp[B_2 t/P_c]$ for each model $([A_2, B_2] = [5.90\times10^{-3}, 7.82\times10^{-2}]$ for model I-i[a], $[5.31\times10^{-3}, 8.35\times10^{-2}]$ for model I-ii[a], and $[5.74\times10^{-3}, 4.20\times10^{-2}]$ for model I-iii[a]).

$$U_m = \frac{1}{2\pi U}\int d\varphi u e^{im\varphi}, \qquad U = \int_V dv u,$$

where $u \equiv H + \Phi = \varepsilon + p/\rho + \Phi$ (Fig. 7). In all three low T/W $n=1$ dynamically unstable stars, the scalar potential contains a single local minimum around $\varpi/r_e \approx 0.2$–0.3, which may express a singular behavior at corotation in pulsation equations. Only a monotonic increase of the potential between corotation and the surface indicates that the dominant frequency we find in simulations represents a fundamental (f) mode in rotating pulsating stars.

Our comparison of characteristic complex frequencies (which represent the oscillation frequencies and the growth times) between three different approaches—a cylindrical model, a spheroidal model, and a numerical simulation—is

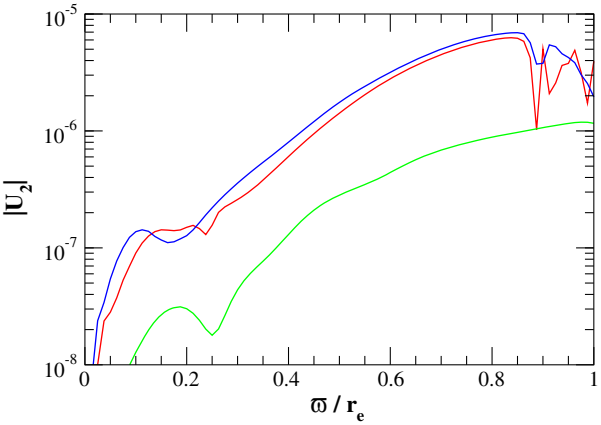

FIG. 7. Scalar potentials $|U_2|$ for three low T/W $n=1$ dynamically unstable stars in the equatorial plane. Red, blue, and green lines, respectively, represent models I-i(a) at $t = 105.6P_c$, I-ii(a) at $t = 88.5P_c$, and I-iii(a) at $t = 102.1P_c$.

TABLE VII. The $m = 2$ unstable f mode of $n = 1$ differentially rotating stars for three different approaches.

Model	Approach	$\Re[\omega]/\Omega_c$	$\Im[\omega]/\Omega_c$	$r_{\rm cr}/r_e$
I(i-a)	Cylinder	0.29017	0.00855	0.48549
I(i-a)	Spheroid	0.35170	0.01684	0.43297
I(i-a)	Simulation	0.380	0.0124	0.412
I(ii-a)	Cylinder	0.36611	0.00975	0.42251
I(ii-a)	Spheroid	0.43019	0.01473	0.38205
I(ii-a)	Simulation	0.458	0.0133	0.367
I(iii-a)	Cylinder	0.51473	0.00862	0.33974
I(iii-a)	Spheroid	0.60222	0.00936	0.30470
I(iii-a)	Simulation	0.622	0.00668	0.296

TABLE VIII. Equilibrium configuration of $n = 1$ differentially rotating stars for verification.

Model	Ω_c/Ω_e	T/W
I-i(a)	26.0	6.09×10^{-2}
I-ii(a)	26.0	3.95×10^{-2}
I-iii(a)	26.0	1.90×10^{-2}

summarized in Table VII. As deformation of the equilibrium star becomes small, the results of a spheroidal model and a numerical simulation approach each other. This feature is especially seen in the corotation radius of the star and the growth rate of the instabilities. In a spherically symmetric background, it is natural to expand the perturbed quantities using a spherical harmonics. As a star deviates from a spherical symmetry, a spheroidal model becomes only an approximation, since the model assumes spherical harmonic dependence. In addition, there is also good agreement of the results between cylindrical and spheroidal models when the deformation rate is small. Since a cylindrical model has less restriction for computing the normal modes in the frequency regions, we mainly explore the results of a cylindrical model in a wide frequency regime and present generic features in Sec. IV B.

B. Numerical simulations

We pick up four low T/W dynamically unstable stars (I[a], II[a], III[a], and IV[a] of Table I), varying the stiffness of the equation of state, to focus on the dominancy of spiral ($m = 1$) and bar ($m = 2$) modes throughout the evolution. Here we impose the following density perturbation in the equilibrium configuration as:

$$\rho = \rho_{\rm eq}\left(1 + \delta^{(1)}\frac{x+y}{r_e} + \delta^{(2)}\frac{x^2+2xy-y^2}{r_e^2}\right),$$

where we set $\delta^{(1)} = \delta^{(2)} = 1 \times 10^{-5}$ to trigger the instabilities. We monitor M_m diagnostics (M_1, M_2, M_3, and M_4)

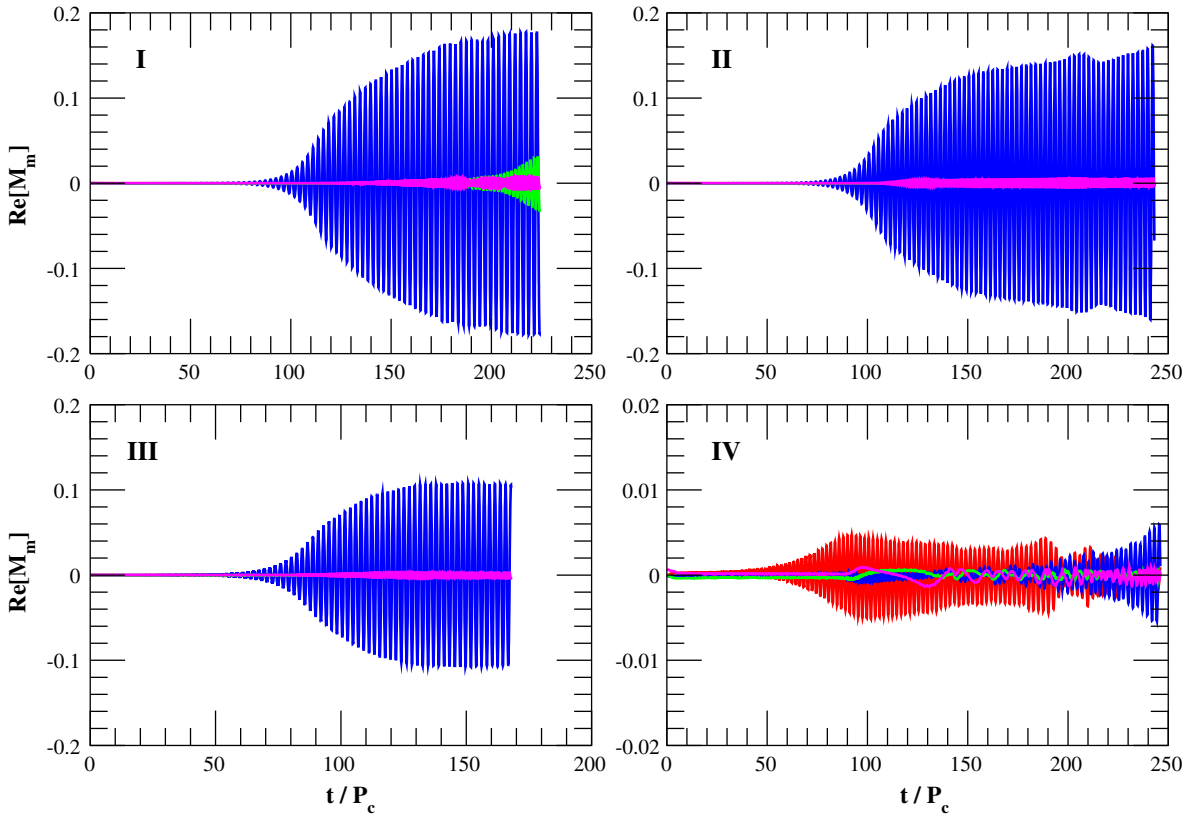

FIG. 8. The M_m diagnostics for four low T/W dynamically unstable stars. Red, blue, green, and magenta lines, respectively, represent diagnostics M_1, M_2, M_3, and M_4.

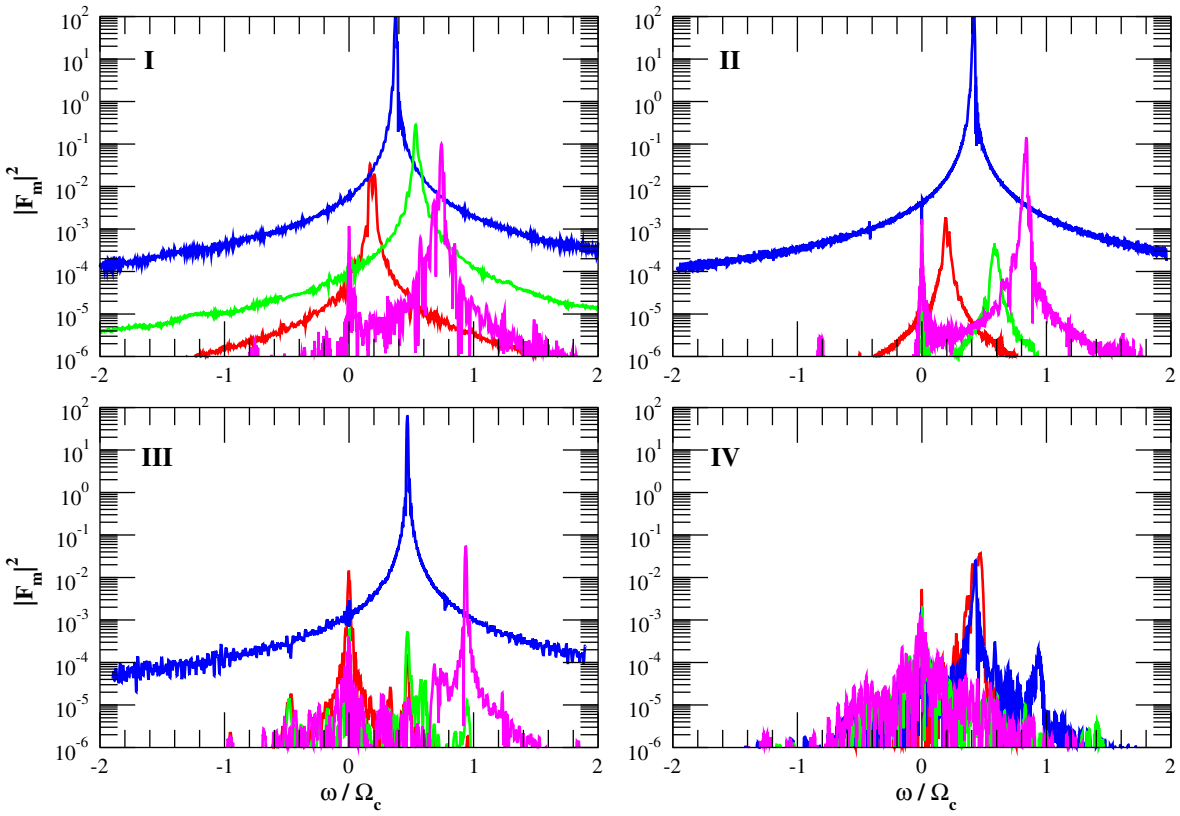

FIG. 9. Spectra of M_m diagnostics ($|F_m|^2$) for four low T/W dynamically unstable stars. Red, blue, green, and magenta lines, respectively, represent $m = 1$, 2, 3, and 4. Only a single dominant peak in the spectrum shows that the unstable stars contain one dominant characteristic frequency.

for all four unstable stars, shown in Fig. 8. For models I, II, and III, the $m = 2$ diagnostics grow exponentially up to $\approx$0.10–0.15, with substantial growth of $m = 4$. Especially for model I, the $m = 3$ diagnostic grows exponentially around $t \gtrsim 180P_c$, which may be explained as a nonlinear mode coupling from the bar mode investigated in Refs. [34,35]. In contrast to the former three models, model IV contains a qualitative difference. The $m = 1$ diagnostic grows exponentially up to $\approx$0.006, with substantial growth of $m = 2$–4 around $t \gtrsim 150P_c$. This feature can be used to restrict the stiffness of the equation of state. This subject will be discussed in Sec. IV D.

We compute the spectra of the diagnostics M_m in Fig. 9. We find a clear peak for each diagnostic. Model I has a peak at $\omega = 0.168\Omega_c$ for $m = 1$, $\omega = 0.375\Omega_c$ for $m = 2$, $\omega = 0.535\Omega_c$ for $m = 3$, and $\omega = 0.742\Omega_c$ for $m = 4$. Model II has a peak at $\omega = 0.191\Omega_c$ for $m = 1$, $\omega = 0.409\Omega_c$ for $m = 2$, $\omega = 0.583\Omega_c$ for $m = 3$, and $\omega = 0.825\Omega_c$ for $m = 4$. Model III has a peak at (no peak for $m = 1$) $\omega = 0.485\Omega_c$ for $m = 2$, $\omega = 0.469\Omega_c$ for $m = 3$, and $\omega = 0.937\Omega_c$ for $m = 4$. From these three models, the M_2 diagnostics take the dominant role as the maximum spectrum amplitude is the highest for all four diagnostics. Also the peak frequency of $m = 4$ is almost twice that of $m = 2$, indicating that they are generated from the same corotation and act as harmonics. In contrast, the odd M_m diagnostics do not have a harmonic behavior to the bar mode, meaning that they are generated from different corotations.

We show scalar potentials U_m for $m = 1$ and $m = 2$ in Fig. 10. Although the definition of a scalar potential has been taken from the feature of a perturbative approach, we clearly find the same behavior even in the results of three-dimensional simulations, indicating a clear correspondence to the existence of corotation.

C. Saturation amplitude and gravitational waves

We compute approximate gravitational waveforms by evaluating the quadrupole formula. In the radiation zone, gravitational waves can be described by a transverse-traceless, perturbed metric h_{ij}^{TT} with respect to a flat spacetime. In the quadrupole formula, h_{ij}^{TT} is found from [36]

$$h_{ij}^{TT} = \frac{2}{r}\frac{d^2}{dt^2} I_{ij}^{TT}, \tag{4.4}$$

where r is the distance to the source, where I_{ij} is the quadrupole moment of the mass distribution [see Eq. (36.42b) in Ref. [36]], and where TT denotes the transverse-traceless projection. Choosing the direction of the wave propagation to be along the x axis (one of the

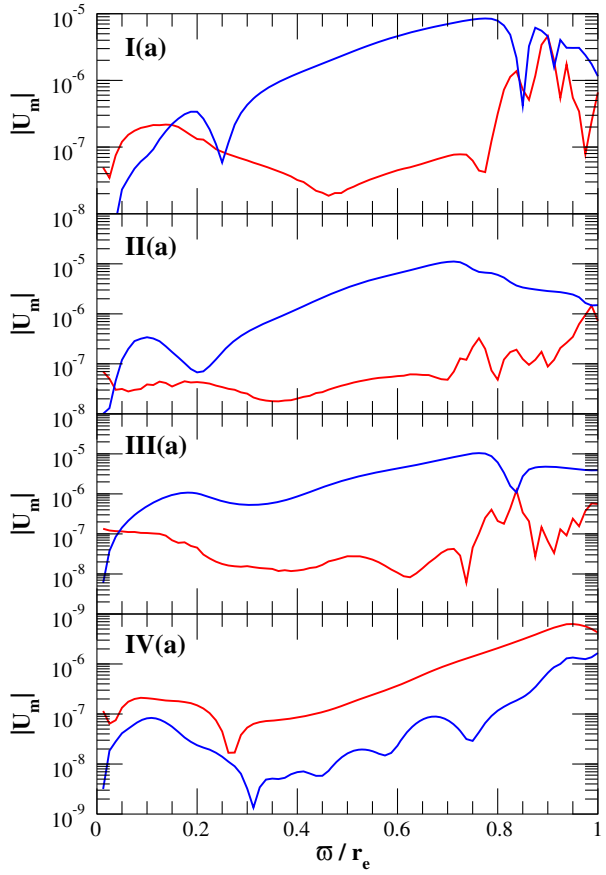

FIG. 10. Scalar potentials of $|U_1|$ (red line) and $|U_2|$ (blue line) diagnostics for four low T/W dynamically unstable stars in the equatorial plane. The potentials are respectively plotted at $t = 171.8P_c$ (model I[a]), at $t = 219.3P_c$ (model II[a]), at $t = 106.75P_c$ (model III[a]), and at $t = 78.11P_c$ (model IV[a]).

principal axes in the equatorial plane of the equilibrium star) and z axis (rotational axis of the equilibrium star), we determine the two polarization modes of gravitational waves from

$$h_+^{(x)} \equiv \frac{1}{2}(h_{yy}^{TT} - h_{zz}^{TT}) \quad \text{and} \quad h_\times^{(x)} \equiv h_{yz}^{TT}, \tag{4.5}$$

$$h_+^{(z)} \equiv \frac{1}{2}(h_{xx}^{TT} - h_{yy}^{TT}) \quad \text{and} \quad h_\times^{(z)} \equiv h_{xy}^{TT}. \tag{4.6}$$

For observers along the x axis and z axis, we thus have

$$\frac{rh_+^{(x)}}{M} = \frac{1}{2M}\frac{d}{dt}(\dot{I}_{yy} - \dot{I}_{zz}), \tag{4.7}$$

$$\frac{rh_\times^{(x)}}{M} = \frac{1}{M}\frac{d}{dt}\dot{I}_{yz}, \tag{4.8}$$

$$\frac{rh_+^{(z)}}{M} = \frac{1}{2M}\frac{d}{dt}(\dot{I}_{xx} - \dot{I}_{yy}), \tag{4.9}$$

$$\frac{rh_\times^{(z)}}{M} = \frac{1}{M}\frac{d}{dt}\dot{I}_{xy}. \tag{4.10}$$

Note that $\dot{A}$ represents the time derivative of A. The number of time derivatives I_{ij} that have to be taken out can be reduced by using the continuity equation [Eq. (2.2)]

$$\dot{I}_{ij} = \int (\rho v^i x^j + \rho x^i v^j) d^3x, \tag{4.11}$$

in Eqs. (4.7), (4.8), (4.9), and (4.10) (see Ref. [37]).

The spectrum of a gravitational waveform can be computed as

$$S = |\tilde{h}_+|^2 + |\tilde{h}_\times|^2, \tag{4.12}$$

where

$$\tilde{h}_{+,\times} = \int dt h_{+,\times} e^{i\omega t}. \tag{4.13}$$

We show gravitational waveforms (Fig. 11) and their spectra (Fig. 12) along the equilibrium rotational axis from four different low T/W dynamically unstable stars. We find quasiperiodic oscillations for all four models for both $+$ and $\times$ modes. Also a single characteristic frequency can be seen in the spectra for all models. For example, $\omega = 0.375\Omega_c$ for model I, $\omega = 0.418\Omega_c$ for model II, $\omega = 0.468\Omega_c$ for model III, and $\omega = 0.429\Omega_c$ for model IV. Since the observer is set along the rotational axis, we can only observe $m(=l) \gtrsim 2$ diagnostics. Therefore, all frequencies of peaks in the spectra correspond to those in $m = 2$ diagnostics.

In order to focus on the detectability of $m = 1$ diagnostics, we next locate the observer along the equatorial plane of the equilibrium stars and show gravitational waveforms (Fig. 13) and their spectra (Fig. 14). In this case, all m modes ($-l \le m \le l$ for each l modes) can be observed. We only find a quasiperiodic oscillation for all four models for $+$ modes, indicating the feature of $m = 2$ diagnostics. We also find an amplified oscillation in $\times$ mode when the $m = 1$ diagnostic grows, indicating one feature of the $m = 1$ diagnostic. This feature can clearly be seen in the spectrum of gravitational waves. Models I and II have two peaks in the spectrum of positive frequency, $\omega = 0.192\Omega_c$, $0.375\Omega_c$ for model I and $\omega = 0.218\Omega_c$, $0.418\Omega_c$ for model II. Comparing to the peak frequencies in the M_m diagnostics, two peak frequencies in the gravitational waveforms respectively correspond to $m = 1$ and $m = 2$ diagnostics. Model III has a single positive frequency $\omega = 0.468\Omega_c$, which corresponds to the $m = 2$ diagnostic. Model IV has four peaks in low amplitudes compared to models I, II, and III, and the peak frequencies are $\omega = 0.190\Omega_c$, $0.417\Omega_c$, $0.610\Omega_c$, and $0.927\Omega_c$.

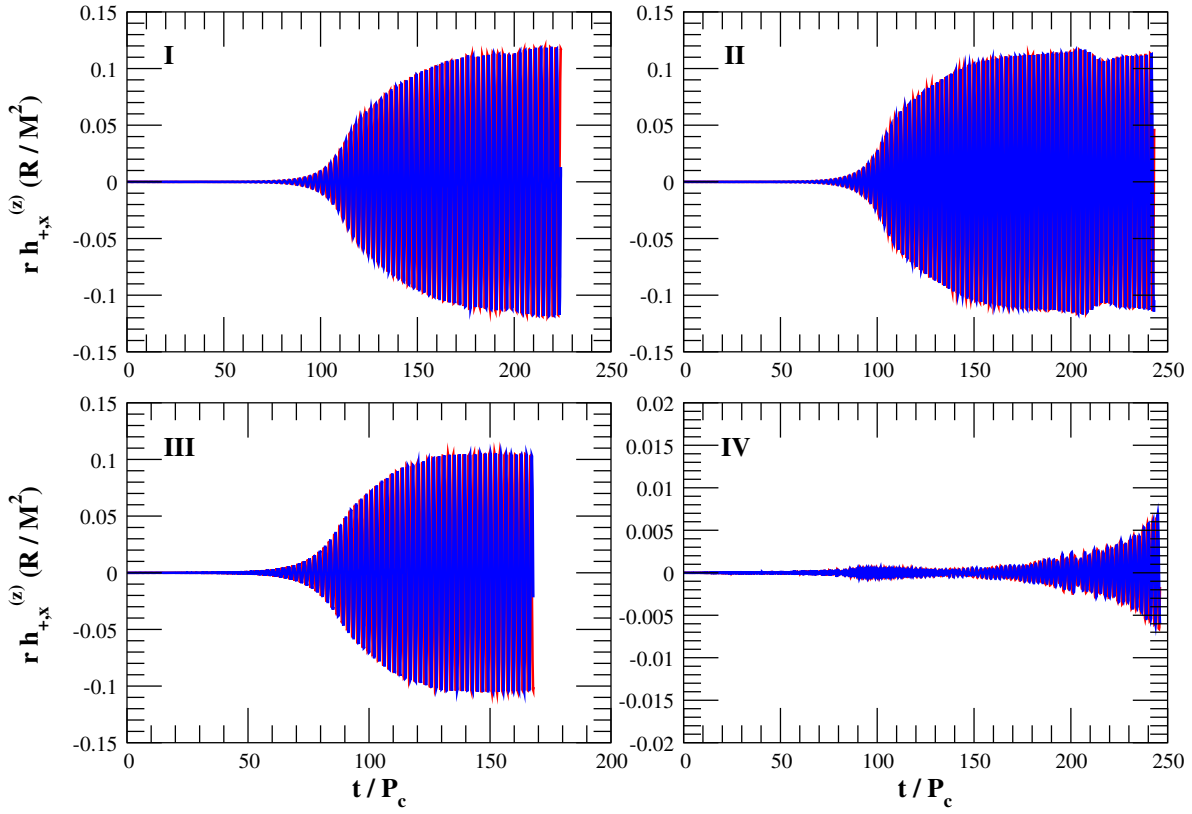

FIG. 11. Gravitational waveforms for four low T/W dynamically unstable stars observed along the rotational axis of the equilibrium star. Red and blue lines, respectively, represent $+$ and $\times$ modes.

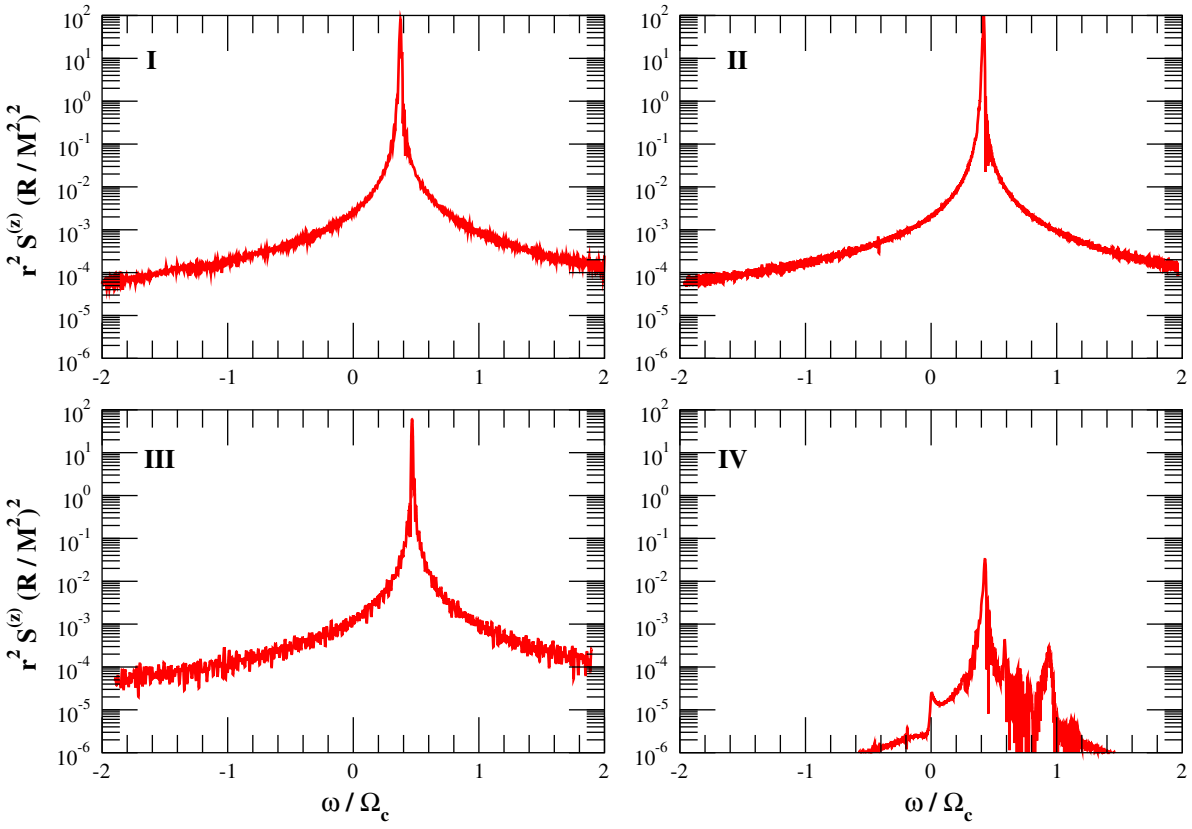

FIG. 12. Spectra of gravitational waveforms observed along the rotational axis for four low T/W dynamically unstable stars.

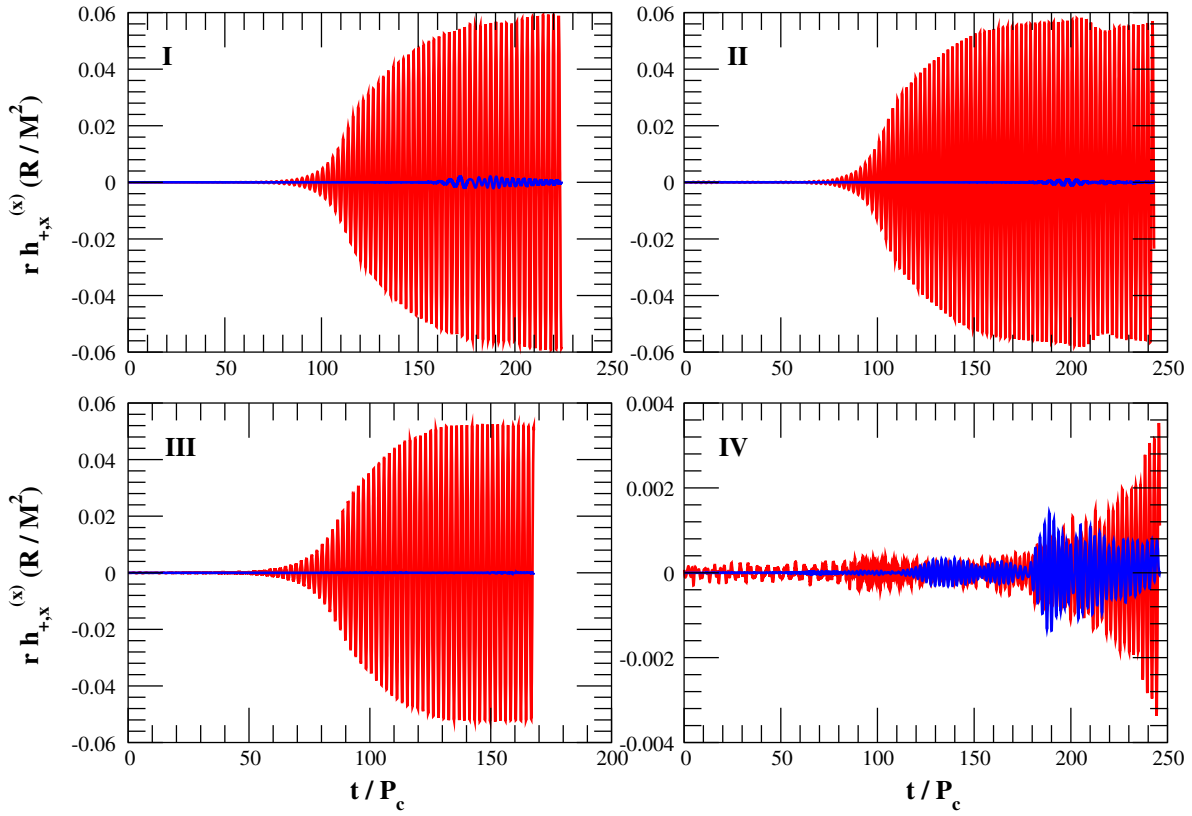

FIG. 13. Same as Fig. 11, but along the principal axis in the equatorial plane.

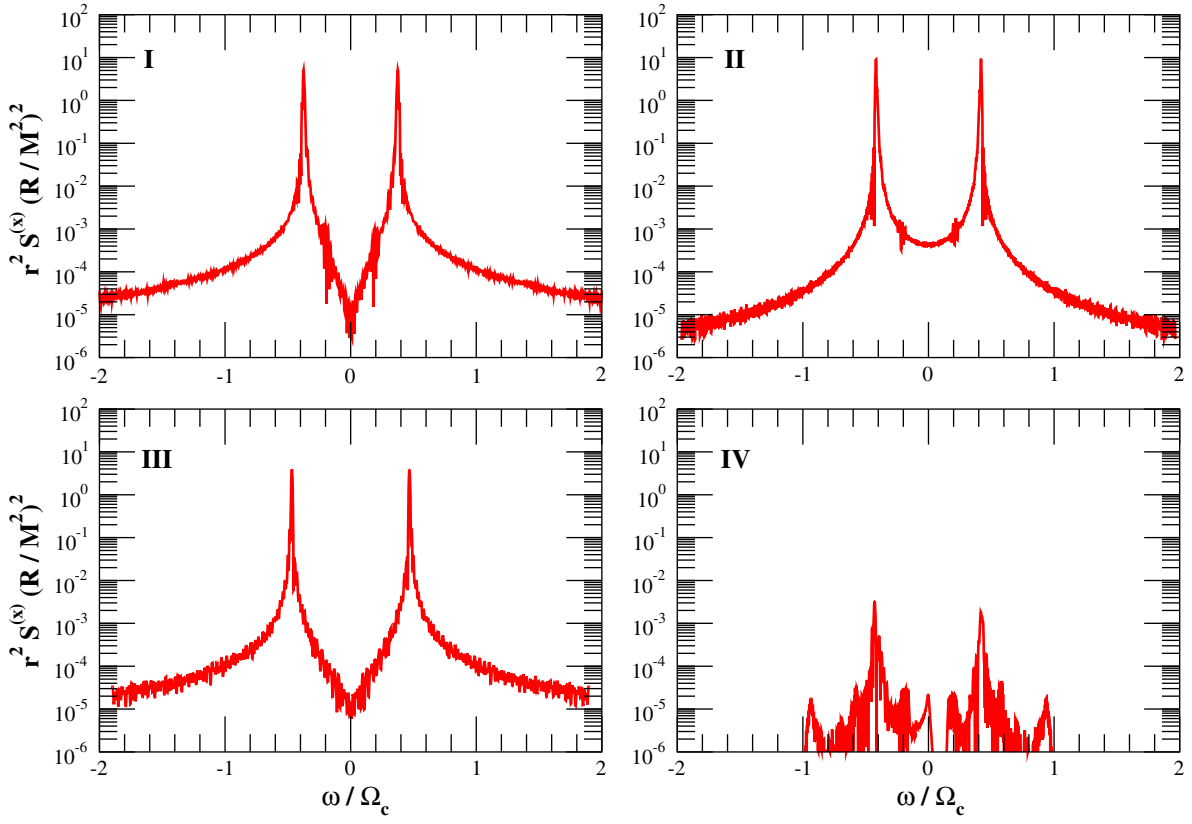

FIG. 14. Same as Fig. 12, but in the equatorial plane.

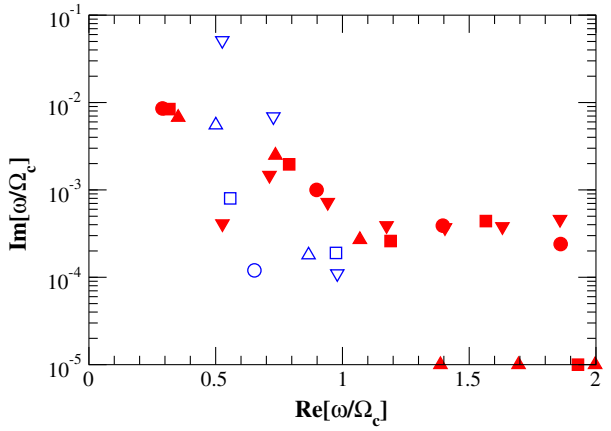

FIG. 15. The $m = 1$ and $m = 2$ eigenfrequencies for four low T/W dynamically unstable stars (models I[a], II[a], III[a], and IV [a]) in cylindrical models. Circles, squares, top triangles, and bottom triangles, respectively, denote the polytropic index of $n = 1$, 1.5, 2, and 3. Opened and filled symbols, respectively, represent the $m = 1$ and $m = 2$ modes. Comparing the largest imaginary frequencies between $m = 1$ and $m = 2$ in each polytropic index, the dominant m mode changes at the stiffness of the equation of state around $\Gamma \approx 1.50$.

D. Constrain the stiffness of the equation of state

Finally we propose one procedure for constraining the stiffness of the equation of state by the direct detection of gravitational waves. We find from three-dimensional numerical simulations that the dominancy mode between $m = 1$ and $m = 2$ throughout the evolution strongly depends on the stiffness of the equation of state (Fig. 8). Models I, II, and III have M_2 diagnostics dominancy, while model IV has M_1 dominancy. We also extract the growth rate of the instabilities from each M_m diagnostic using the same fitting formula as in Sec. IV A but changing the starting time t_0 of the exponential growth as

$$M_m = A_m \exp\left[B_m(t - t_0)/P_c\right]. \tag{4.14}$$

Note that we extract two constants A_m and B_m through around 50 central rotation periods of the equilibrium stars from time t_0. The imaginary part of complex characteristic frequencies of model I are $\Im[\omega]/\Omega_c = 0.0109$, $t_0 = 160P_c$ for $m = 1$ and $\Im[\omega]/\Omega_c = 0.0168$, $t_0 = 50P_c$ for $m = 2$; model II are $\Im[\omega]/\Omega_c = 0.00557$, $t_0 = 170P_c$ for $m = 1$ and $\Im[\omega]/\Omega_c = 0.0179$, $t_0 = 50P_c$ for $m = 2$; model III are $\Im[\omega]/\Omega_c = 0.00366$, $t_0 = 120P_c$ for $m = 1$ and $\Im[\omega]/\Omega_c = 0.0175$, $t_0 = 40P_c$ for $m = 2$; and model IV are $\Im[\omega]/\Omega_c = 0.00909$, $t_0 = 40P_c$ for $m = 1$ and $\Im[\omega]/\Omega_c = 0.00459$, $t_0 = 150P_c$ for $m = 2$. Therefore, a clear relation between the dominancy of the saturation amplitude of M_m diagnostics and the strength of the characteristic complex frequency can be seen in Fig. 8. There seems to be a threshold between $\Gamma = 1.33$ and 1.5 to change the dominancy of the m mode. This feature can roughly be understood from the strength of the instabilities by investigating the imaginary part of the eigenfrequency. Evaluating the amplification timescale derived in Eq. (3.41) for each eigenfrequency computed in Tables II, III, IV, and V, the imaginary part of the reflection eigenfrequency has a clear dependence on the stiffness of the equation of state. We summarize our finding in Fig. 15.

V. CONCLUSIONS

We have investigated the unstable features of low T/W dynamical instabilities in differentially rotating stars in terms of a wide range of the stiffness of the equation of state. We have adopted a normal mode analysis and a scattering rising from the corotation barrier in the equatorial plane, and compare the results with those of three-dimensional hydrodynamic simulations.

Unstable normal modes for low T/W dynamically unstable stars are found in the linear analysis, and they are qualitatively confirmed by an amplified oscillation of the scattering sound waves between corotation and the surface. Although the growth timescale is in agreement on a qualitative level, the criterion has clear agreement with the results of both numerical simulations and normal mode analyses. We do not find any additional modes to the well-known f and p modes in the linear analysis for both stable and unstable stars, but the stability of the system may change when the corotation barrier appears in the effective potential. The resonant frequency in both cylindrical and spheroidal models in the linear analyses agrees with that of hydrodynamic simulations when the deformation rate of the rotating configuration approaches zero (nonrotating configuration). The above fact confirms our models to be efficient for finding low T/W dynamically unstable stars.

The eigenfunction of the modes is also found to display a similar behavior to the well known f and p modes. Once corotation exists inside the star, the perturbed enthalpy oscillates between corotation and the surface. This may indicate that the perturbed enthalpy is affected by the corotation barrier, and therefore cannot cross corotation. This feature requires reinterpretation of the pulsation modes in rotating stars when a corotation singularity exists inside the stars.

Finally we are able to constrain the stiffness of the equation of state by the direct observation of mode decomposed gravitational waves from low T/W dynamically unstable stars. Investigating the dominancy of the azimuthal mode in the normal mode analysis in a cylindrical model, the threshold of the $m = 2$ bar mode is around $\Gamma \approx 1.50$. Using the above fact, we are able to constrain the stiffness of the equation of state by focusing the ratio between $m = 1$ and $m = 2$ of the gravitational waveform.

We have computed the linear analysis in the equatorial plane to reduce the basic pulsation equations to the ordinary differential ones. Our results clearly show that a rotational configuration of the star should be fully taken into account. In order to achieve complete agreement between the linear

analysis and hydrodynamic simulation, a two-dimensional eigenmode analysis with corotation duly considered is required, which is a challenging task in this field.

ACKNOWLEDGMENTS

This work was supported in part by JSPS Grant-in-Aid for Young Scientists B (No. 23740201), Grant-in-Aid for Scientific Research B (No. 16H03986), and by the Waseda University Grant for Special Research Projects (No. 2014K-6100). Numerical computations were performed on the Cray XC40 cluster in the Yukawa Institute for Theoretical Physics, Kyoto University, on the Cray XC30 cluster in the Center for Computational Astrophysics, National Astronomical Observatory of Japan, and on the cluster at Relativistic Astrophysics Group at the Research Institute for Science and Engineering, Waseda University, and at High Energy Astrophysics Group at Department of Physics, Waseda University.

APPENDIX: BOUNDARY CONDITION AT CENTER IN SPHEROIDAL MODELS

We adopt the technique of Unno *et al.* [23] for imposing a regularity condition at the center. The basic pulsation equations at the center can be written as

$$r\frac{d}{dr}\begin{bmatrix}\delta U_{lm}\\ \chi_{lm}\\ \delta\Phi_{lm}\\ \psi_{lm}\end{bmatrix}=\begin{bmatrix}0 & 1 & 0 & 0\\ \alpha_{lm} & \beta_{lm} & 0 & 0\\ 0 & 0 & 0 & 1\\ 0 & 0 & l(l+1) & -1\end{bmatrix}\begin{bmatrix}\delta U_{lm}\\ \chi_{lm}\\ \delta\Phi_{lm}\\ \psi_{lm}\end{bmatrix}, \tag{A1}$$

where $\chi_{lm}=r(d\delta U_{lm}/dr)$, $\psi_{lm}=r(d\delta\Phi_{lm}/dr)$,

$$\alpha_{lm}=l(l+1)-q_{lm}[l(l+1)-m^2], \tag{A2}$$

$$\beta_{lm}=-1+q_{lm}, \tag{A3}$$

$$q_{lm}=\frac{4\Omega_c^2}{\tilde{\omega}^2}. \tag{A4}$$

The four eigenvalues of the matrix in Eq. (A1) are

$$\lambda_{lm}=\lambda_{lm}^{(1)},\qquad \lambda_{lm}^{(2)},\qquad l,\qquad -(l+1),$$

where $\lambda_{lm}^{(1)}$ and $\lambda_{lm}^{(2)}$ satisfy

$$\lambda_{lm}^2-\beta_{lm}\lambda_{lm}-\alpha_{lm}=0. \tag{A5}$$

It is clear from the matrix in Eq. (A1) that the real parts of the eigenvalues $\lambda_{lm}^{(1)}$ and $\lambda_{lm}^{(2)}$ correspond to the powers of δU_{lm} and χ_{lm} at the center, while l and $-(l+1)$ correspond to those of $\delta\Phi_{lm}$ and ψ_{lm}.

In order to close the system as an eigenvalue problem, only 2 out of 4 degrees of freedom at the center are needed since 1 freedom represents scaling for the whole system, and the other freedom represents the one of a surface boundary condition. Since the power $-(l+1)$ for $\delta\Phi_{lm}$ is already discarded because of the regularity condition at the center ($l\gtrsim 0$), only one of the powers $\lambda_{lm}^{(1)}$ or $\lambda_{lm}^{(2)}$ for δU_{lm} should be discarded. The above condition can be written in general as

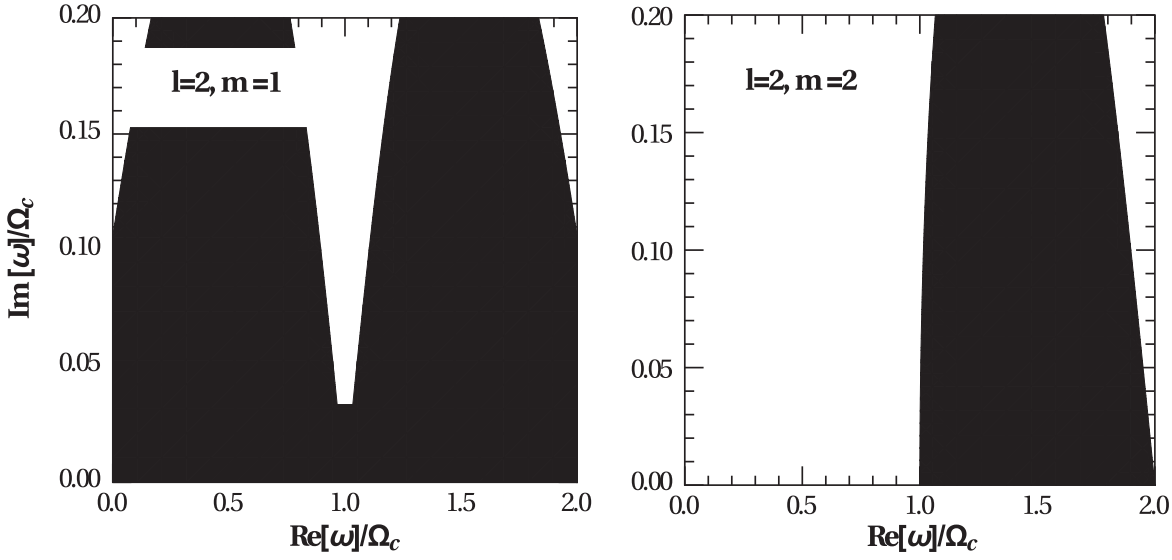

FIG. 16. Allowed frequency region (white region) to treat the pulsation system for spheroidal models as an eigenvalue problem. The left panel represents the case of $l=2$, $m=1$, and the right one represents that of $l=2$, $m=2$.

$$\max(\Re[\lambda_{lm}^{(1)}], \Re[\lambda_{lm}^{(2)}]) \geq 1, \qquad \min(\Re[\lambda_{lm}^{(1)}], \Re[\lambda_{lm}^{(2)}]) < 1. \tag{A6}$$

Therefore, we restrict the frequency regime with the above condition. We show the allowed frequency region for the case of $l = 2$, $m = 1$ and 2 in Fig. 16.

Finally, the regularity conditions at the center are written as

$$\delta U_{lm} = C_{lm}^1 r^{\max(\Re[\lambda_{lm}^{(1)}], \Re[\lambda_{lm}^{(2)}])}, \qquad \delta\Phi_{lm} = C_{lm}^2 r^l,$$

where C_{lm}^1 and C_{lm}^2 are constants.

[1] B. K. Pickett, R. H. Durisen, and G. A. Davis, Astrophys. J. **458**, 714 (1996).
[2] J. M. Centrella, K. C. B. New, L. L. Lowe, and J. D. Brown, Astrophys. J. **550**, L193 (2001).
[3] M. Shibata, S. Karino, and Y. Eriguchi, Mon. Not. R. Astron. Soc. **334**, L27 (2002); **343**, 619 (2003).
[4] M. Saijo, T. W. Baumgarte, and S. L. Shapiro, Astrophys. J. **595**, 352 (2003).
[5] S. Chandrasekhar, *Ellipsoidal Figures of Equilibrium* (Yale University Press, New Haven, CT, 1969), Chap. 5.
[6] J.-L. Tassoul, *Theory of Rotating Stars* (Princeton University Press, Princeton, NJ, 1978), Chap. 10.
[7] S. L. Shapiro and S. A. Teukolsky, *Black Holes, White Dwarfs, and Neutron Stars: The Physics of Compact Objects* (Wiley-Interscience, New York, 1983), Chap. 7.5.
[8] M. Saijo and S.-i. Yoshida, Mon. Not. R. Astron. Soc. **368**, 1429 (2006).
[9] S. Ou and J. E. Tohline, Astrophys. J. **651**, 1068 (2006).
[10] V. Paschalidis, W. E. East, F. Pretorius, and S. L. Shapiro, Phys. Rev. D **92**, 121502 (2015).
[11] W. E. East, V. Paschalidis, F. Pretorius, and S. L. Shapiro, Phys. Rev. D **93**, 024011 (2016).
[12] L. Lehner, S. L. Liebling, C. Palenzuela, and P. M. Motl, Phys. Rev. D **94**, 043003 (2016).
[13] D. Radice, S. Bernuzzi, and C. D. Ott, Phys. Rev. D **94**, 064011 (2016).
[14] H. Dimmelmeier, J. A. Font, and E. Müller, Astron. Astrophys. **388**, 917 (2002); **393**, 523 (2002).
[15] T. Kuroda, T. Takiwaki, and K. Kotake, Phys. Rev. D **89**, 044011 (2014).
[16] C. D. Ott, H. Dimmelmeier, A. Marek, H.-T. Janka, I. Hawke, B. Zink, and E. Schnetter, Phys. Rev. Lett. **98**, 261101 (2007).
[17] D. Lynden-Bell and A. J. Kalnajs, Mon. Not. R. Astron. Soc. **157**, 1 (1972).
[18] A. L. Watts, N. Andersson, and D. I. Jones, Astrophys. J. **618**, L37 (2005).
[19] R. V. E. Lovelace, H. Li, S. A. Colgate, and A. F. Nelson, Astrophys. J. **513**, 805 (1999).
[20] G. Corvino, L. Rezzolla, S. Bernuzzi, R. De Pietri, and B. Giacomazzo, Classical Quantum Gravity **27**, 114104 (2010).
[21] S. Karino and Y. Eriguchi, Astrophys. J. **592**, 1119 (2003).
[22] A. Passamonti and N. Andersson, Mon. Not. R. Astron. Soc. **446**, 555 (2015).
[23] W. Unno, Y. Osaki, H. Ando, H. Saio, and H. Shibahashi, *Nonradial Oscillations of Stars* (University of Tokyo Press, Tokyo, 1989), Chap. III, Sec. 14.
[24] M. Saijo and S.-i. Yoshida, Phys. Rev. D **94**, 084032 (2016).
[25] S.-i. Yoshida and M. Saijo, Mon. Not. R. Astron. Soc. **466**, 600 (2017).
[26] N. Andersson *et al.*, Classical Quantum Gravity **30**, 193002 (2013).
[27] B. Abbott *et al.*, Phys. Rev. Lett. **119**, 161101 (2017); Astrophys. J. **848**, L13 (2017).
[28] The speed of light only enters through the quadrupole formula of gravitational waves.
[29] R. J. LeVeque, in *Computational Methods for Astrophysical Fluid Flow*, edited by R. J. LeVeque, D. Mihalas, E. A. Dorfi, and E. Müller (Springer, Berlin, 1998).
[30] E. F. Toro, *Riemann Solvers and Numerical Methods for Fluid Dynamics: A Practical Introduction* (Springer Science & Business Media, New York, 2009), Chap. 10.
[31] J. R. Ipser and L. Lindblom, Phys. Rev. Lett. **62**, 2777 (1989).
[32] D. Tsang and D. Lai, Mon. Not. R. Astron. Soc. **387**, 446 (2008).
[33] J. R. Ipser and L. Lindblom, Astrophys. J. **355**, 226 (1990).
[34] M. Saijo and Y. Kojima, Phys. Rev. D **77**, 063002 (2008).
[35] Y. Kojima and M. Saijo, Phys. Rev. D **78**, 124001 (2008).
[36] C. W. Misner, K. S. Thorne, and J. A. Wheeler, *Gravitation* (W. H. Freeman, San Francisco, 1973), Chap. 36.10.
[37] L. S. Finn, in *Frontiers in Numerical Relativity*, edited by C. R. Evans, L. S. Finn, and D. W. Hobill (Cambridge University Press, Cambridge, 1989), pp. 126.